Prussian Blue Based Vertical Graphene 3D Structures for High Frequency Electrochemical

Capacitors

Wenyue Li, Sakibul Azam, Guangzhen Dai, Zhaoyang Fan*

Department of Electrical and Computer Engineering and Nano Tech Center, Texas Tech

University, Lubbock, TX, 79409, USA

*Corresponding author: zhaoyang.fan@ttu.edu

Abstract

Kilohertz high frequency electrochemical capacitors (HF-ECs), with a compact size, are

being actively investigated with the aim for line-frequency ripple current filtering and other

applications. However, the reported performance, particularly achievable capacitance density,

the frequency response, and the phase angle that are directly determined by the electrode

structure is still far from satisfactory that hinders its practical application prospect. In this work,

metal organic framework (Prussian Blue, PB) is introduced as a structural mediator to develop

three-dimensional vertical graphene architecture, or edge-oriented graphene (EOG) on a current

collector via a 5-minutes rapid plasma carbonization and deposition process. With several

prominent merits integrated together in the resulted EOG electrode structure, HF-ECs exhibit

very low equivalent series resistance (ESR) of 40 mΩ cm⁻² and attractive cell capacitance of 1.02

mF cm⁻² and phase angle of -85.9° or 2.34 mF cm⁻² and -80.6° at 120 Hz, which are the best

reported overall performances thus far. Integrated cell is also assembled to work higher voltage

for line-frequency ripple filtering, with demonstrated excellent performance. This study provides

a new method and structure for developing high-performance HF-ECs.

Keywords: electrochemical capacitor, AC filtering, vertical graphene, metal organic framework,

Prussian blue

1

Introduction

Aluminum electrolytic capacitors (AECs), with their largest capacitance among all the conventional dielectric capacitor technologies, are widely used for functions such as current ripple filtering in AC/DC and DC/DC energy conversion, power conditioning, coupling and decoupling in circuits. In the past decade, there have been strong interest in developing kHz high-frequency electrochemical capacitors (HF-ECs) that have even much larger capacitance density and therefore reduced device size in substitution of the bulky AECs[1-7]. Preliminary functional demonstrations of HF-ECs for ripple filtering in AC-DC conversion[8, 9], arbitrary wave filtering[9, 10], low-pass filters and relaxation oscillators[11]have been reported.

Different from dielectric capacitors that can pass AC currents at reasonable frequencies, the conventional ECs were developed for energy storage, with capacitance densities higher than AECs by several orders of magnitude, but with very limited frequency response ($< \sim 1 \text{Hz}$). To produce HF-ECs that can respond at hundreds and even kHz range aiming at line-frequency or even higher frequency filtering, the tortuous mesoporous electrode used in ECs must be replaced with a relatively straightforward and large pore-based structure, and the whole electrode resistance must be reduced[1, 2]. We emphasize that area capacitance density at 120 Hz (C_A^{120}), the absolute phase angle value at 120 Hz (Φ_{120}), and the characteristic frequency when the phase angle reaching -45° (f_0), among others, are considered as the key parameters in evaluating the electrode performance for HF-ECs. From the point of view of engineering, dissipation factor (DF) or the loss tangent (Figure S1a) is also critical, which determines how much the energy entering the capacitor will be dissipated as heat. For commercial AECs at 120 Hz, DF is limited to $\leq 14\%$ or $\Phi_{120} \geq 82^{\circ}$ for small capacitance, while DF $\leq 8.7\%$ or $\Phi_{120} \geq 85^{\circ}$ for large capacitance. Therefore, we recommend that the so-called AC-filtering EC should at least meet $\Phi_{120} \geq 80^{\circ}$.

Vertical graphene (VG) grown on a nickel foil in a plasma-enhanced chemical vapor deposition (PECVD) was the electrode structure used in the first reported HF-EC that showed adequate frequency response at tens of kHz[1]. To overcome the limited areal capacitance caused by a very thin VG layer ($< \sim 1 \mu m$) grown on a flat metal foil[12-14], three-dimensional (3D) scaffold networks for edge-oriented vertical graphene (EOG) growth were further reported[4, 15, 16]. Other carbon and non-carbon-based nanostructures are also being investigated to achieve high-frequency response at a large capacitance density[17-24]. Several recent works reported using crosslinked carbon nanofibers[9], carbon nanotubes[25-28], graphene nanomesh film[29], CMK-5[30], MXene[5, 6], metal sulfides[31], PEDOT[10]and other materials or structures[32, 33] as electrodes. In a few works, very large capacitance density was reported but the corresponding Φ_{120} was far low than 80° to meet the expectation for a good filtering capacitor.

Despite the steady progress, only a few studies reported electrodes that meet the minimum requirements of $f_0 > 1$ kHz, $\Phi_{120} > 80^{\circ}$ and a reasonable $C_A^{120} > 0.5$ mF cm⁻², while better electrodes with larger capacitance were only reported very recently using PEDOT-derived carbon[24], the bacterial cellulose(BC)-derived crosslinked carbon nanofibers(CCNF)[9] and carbon black coated VG[23]. Other novel structures for HF-EC with large C_A^{120} need to be further explored.

Metal organic frameworks (MOFs), with adjustable structure and components, have the potency as a category of raw materials to synthesize functional carbon-based nanomaterials[34-36]. If properly processed, the derived carbon products could maintain the polyhedral shapes of the original MOFs, making these versatile 'bricks' capable of building 3D conductive networks with macro-scale pores interlaced[37]. We hypothesized that such a novel 3D network could be the framework for growing EOG to achieve an outstanding electrode for large capacitance, low

resistance and high frequency response. Inspired by this idea, herein, we report the study of using Prussian blue (PB) cubes with tunable sizes as a precursor to derive the 3D conductive porous network for EOG deposition. In a rapid (< 7 minutes) plasma-enhanced chemical vapor deposition (PECVD) process, the PB cube layer coated on a current collector was converted into Fe₃C-nanoparticle/carbon-based core/shell cubes that were further covered by EOG nanosheets. A seamless interface between the current collector and these active materials was simultaneously formed. Benefiting from these characteristics, the fabricated kHz cells exhibited equivalent series resistance (ESR) as low as 40 m Ω cm⁻², Φ_{120} = 85.9° and C_A^{120} = 1.02 mF cm⁻², or Φ_{120} = 80.6° and C_A^{120} = 2.34 mF cm⁻², which are among the best reported overall performances thus far. Integrated cell was assembled to work at 2.7 V for line frequency ripple filtering of different waveforms, demonstrating excellent performance.

Results and Discussion

Prussian blue (PB) is a dark blue pigment with the chemical formulate Fe^{III}₄[Fe^{II}(CN)₆]₃. Its cubic lattice and the whole process to fabricate the electrode is schematically illustrated in Figure 1a, where photo images of PB powder, its coating on a stainless-steel (SS) current collector, and after plasma treatment are also shown. As detailed in the Experimental section in the Supplement Information (SI), PB MOF cubes were synthesized with potassium ferricyanide (K₄Fe(CN)₆·3H₂O) and polyvinylpyrrolidone (PVP) dissolved in HCl solution and then aged at 80 °C for 24 hr [38]. In this synthesis, PVP acts as a structural modifier, adjusting the size of PB cubes through the coordinating interactions between iron ions and amide moieties. As revealed by scanning electron microscopy (SEM) images in Figure S3, the size of PB cubes and their uniformity tend to increase as more PVP is added into the potassium ferricyanide solution. To

preserve substantial surface area for the subsequent EOG growth, PB cubes synthesized with 3 g PVP (size $< 1 \mu m$, Figure 1c) was adopted in this work.

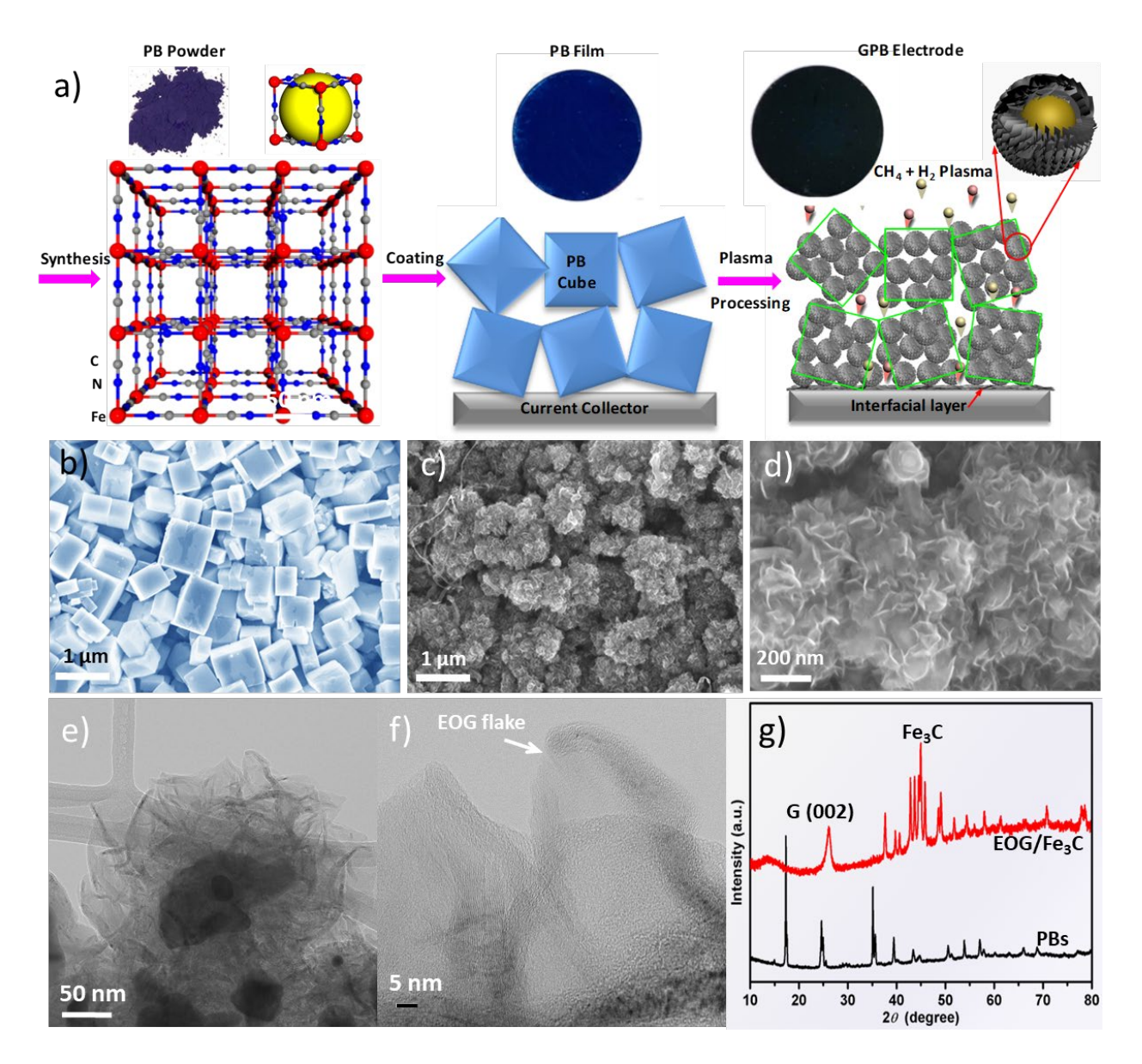


Figure 1. (a) Schematics of the PB lattice structure and the electrode preparation process. SEM images of (b) PB cubes and (c, d) carbonized PB cubes with EOG deposition. (e, f) TEM images of 3-GPB-5 sample. (g) XRD patterns of PB cubes and 3-GPB-5 sample.

The synthesized PB cubes were casted on SS disks into a thin-film, and then treated in a rapid high-temperature CH₄/H₂ plasma process[15, 39] for 3, 5, or 7 minutes, designated as 3-GPB-3, 3-GPB-5, and 3-GPB-7 respectively, for the corresponding samples. This rapid plasma process carbonized PB cubes into interconnected conductive particles, and meanwhile a thin layer of EOG was deposited along the surface profile of these particles. The SEM image in Figure 1c shows the morphology of 3-GPB-5. Due to the decomposition of PB cubes at high temperature and the growth of graphene nanosheets, their cubical shape was partly altered, but the granular morphology was still maintained (Figure S4). The enlarged SEM image in Figure 1d clearly shows the edge-oriented preference of these graphene nanosheets, with particles converted from PB cubes being encapsulated by these nanosheets. Comparatively, only carbon coated nanoparticles can be observed in those samples (Figure S5) which were pyrolyzed in the same condition but without directly exposing to the CH₄ and H₂ plasma. The imaging contrast in these carbonized PB also indicates that particles converted from PB cubes have a similar core/shell structure.

Miniaturization of the whole electrode resistance, including the material resistance and the contact resistance between the current collector and the electrode material, is critical for achieving high frequency response (Figure S2). For solution casted electrodes, a large interfacial resistance typically appears between the current collector and the electrode layer. Interestingly, the cross-sectional view of the 3-GPB-5 sample (Figure S6) reveals that the SS substrate is fused together with the GPB by graphene nanosheets, which were grown at the interface due to plasma species penetration through the large orifices between cubes to the interface, as schematically depicted in Figure 1a. This intimate interfacial connection *via* graphene or graphite sheets would result in much reduced interfacial resistance. Transmission electron microscopy (TEM) images

(Figure 1e, f) further reveal the microstructural details of the 3-GPB-5 sample. The particles converted from PB cubes are well wrapped inside carbon layers, on which graphene nanosheets were grown. The nanosheets consist of multilayer graphene. To identify those particles revealed in SEM and TEM imaging, the XRD pattern of 3-GPB-5 is compared with that of the pristine PB cubes in Figure 1g. After carbonization and EOG growth, a new peak located at 2θ - 26° appeared, which is assigned to graphite (002) crystal plane [40]. Other peaks, especially those appearing in the range of 40-60° are identical to orthorhombic Fe₃C structure[27, 41]. Thanks to this wellconstructed core/shell structure, the Fe₃C core is expected to be stable even in corrosive electrolytes such as a KOH solution. Raman characterization was also carried out and the results are shown in Figure S7, the characteristic peaks located at 1350, 1588 and 2702 cm⁻¹ are derived from the D, G and 2D bands of graphite materials, representing breathing mode of sp² carbon rings, planar configuration sp² bonded carbon and a second order of the D band (or an overtone of the D band), respectively[42]. The extension of exposing time in PECVD results in the slightly increased I_G/I_D value, which can be ascribed to the improvement of the graphitization degree in the 3-GPB-7 sample.

These material studies reveal the structure features illustrated in Figure 1a. The PB cube (~ 1 µm scale) is decomposed at a high temperature forming interconnected Fe₃C/C core/shell submicrometer (~ 100 nm scale) particles, but the overall profile of the original cube is maintained so that large orifices between cubes still exist. The smaller particles in the cube increase the available surface for EOG deposition, and the enlarged EOG surface area will increase the attainable EDLC capacitance density. The interlaced orifices between cubes ensure plasma easily penetrating deeply to deposit EOG along the whole thickness of the Fe-C scaffold and to fuse the current collector with the top structure through interfacial layer deposition. During the capacitor

operation, these orifices will also act as local electrolyte reservoirs for rapid double layer formation thus allowing fast response at high frequencies. Furthermore, each particle is encapsulated with a carbon layer and further coated with EOG, thus forming EOG-C/Fe₃C shell/core structure. The EOG-C shell will reduce the whole electrode resistance and also isolate the Fe-containing core from reacting with the electrolyte, thus preventing occurrence of the slow pseudocapacitive phenomenon. In comparison with much smaller Fe₃C/C nanoparticles converted from PB cubes when carbonized in a slow thermal process that typically runs for several hours[43-45], which does not allow plasma penetrating deep into the film for EOG deposition, the rapid plasma-based carbonization results in sub-micrometer scale particles with large voids between cubes suitable for EOG coating. All these features, working together, ensure this rationally designed electrode structure to attain an outstanding performance, as will be demonstrated.

To further elucidate the structural evolution by plasma treatment, the three samples treated in the plasma for 3, 5, and 7 min were comparatively studied. Their SEM images are shown in Figure 2a-c and S4. For the 3-GPB-3 sample, besides the small EOG flakes, some bare Fe₃C/C particles were still noticeable. With the time duration of plasma treatment extended to 5 min, these particles are completely buried in the newly grown EOG flakes (Figure 2b). For 7 min treatment, EOG nanosheet size expands observably (Figure 2c). The height or size of the EOG flakes is proportional to the treatment time, but much large sheets could increase the porous-electrode behavior and thus limiting the cell frequency response.

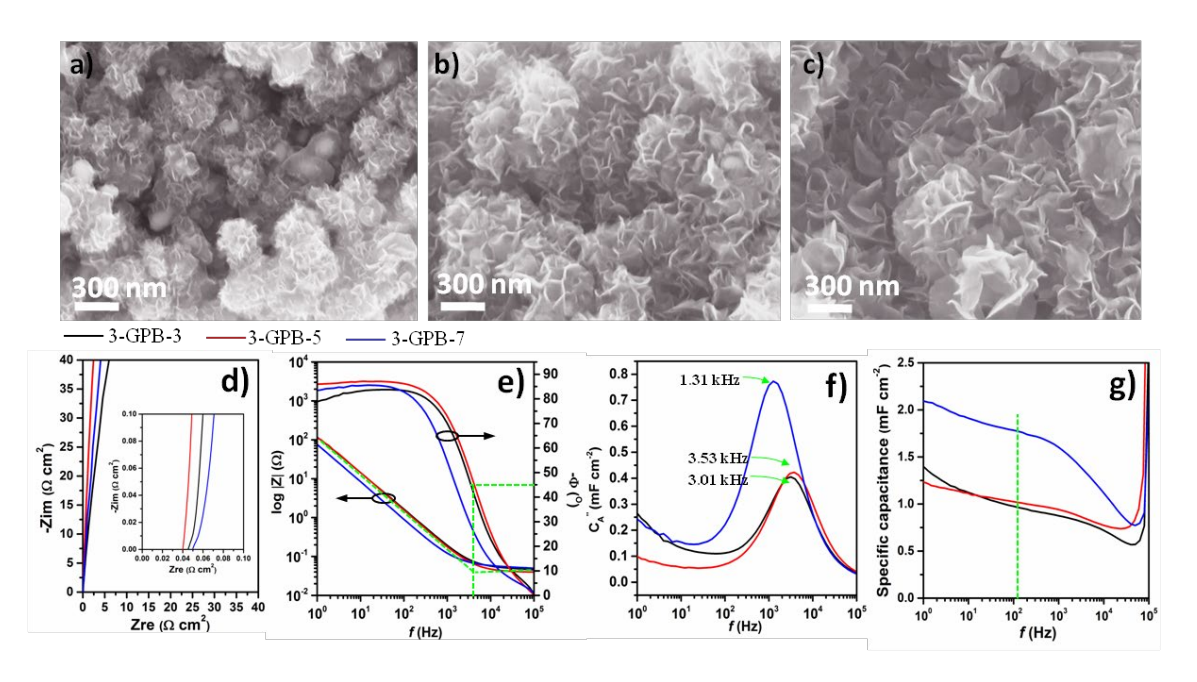


Figure 2. SEM images of 3-GPB-3 in (a), 3-GPB-5 in (b), and 3-GPB-7 in (c). EIS spectroscopic studies of cells based on the three electrodes: complex-impedance-plane plots in (d) with inset displaying the high-frequency region, impedance Bode diagrams in (e), the resonant frequency from the derived imaginary component of the complex capacitance (f), and the derived specific capacitance versus frequency (g). In (g), the derived capacitance based on *RC* series circuit model is accurate only up to the corresponding knee frequency.

Table 1. Comparison of cell performance for two groups of electrodes: 3-GPB-X with the same amount of GPB loading but different plasma processing times, and X-GPB-5 with the same optimized plasma processing time but different GPB loadings.

Electrode	ESR	Ф120	DF ₁₂₀	f_{θ}	C_A^{120}
	$(m\Omega \text{ cm}^2)$	(°)	(%)	(kHz)	(mF cm ⁻²)
3-GPB-3	50	83.2	11.9	3.01	0.96
3-GPB-5	40	85.9	7.17	3.53	1.02
3-GPB-7	55	82.0	14.0	1.45	1.72
3-GPB-5	40	85.9	7.17	3.53	1.02
4-GPB-5	85	80.6	16.6	1.01	2.34
5-GPB-5	200	62.1	52.9	0.25	2.82

To reveal the correlation between the structure and electrochemical performance of samples treated for different plasma durations, symmetrical cells using samples 3-GPB-3, 3-GPB-5, and 3-GPB-7 as electrodes were assembled with 6 M KOH as the electrolyte. Their performance was evaluated via electrochemical impedance spectroscopy (EIS) study and the derived parameters are compared in Table 1. In the complex-impedance-plane plot (Figure 2d), all the spectra show nearly vertical lines and are free of an obvious semi-circle feature at the high frequency region, which is usually caused by either the interfacial resistance between the electrode material and the current collector or pseudocapacitive charge transfer resistance in the electrode. The porous effect is also trivial. 3-GPB-3 and 3-GPB-7 show a knee frequency of 25 kHz and 16 kHz, respectively, while 3-GPB-5 does not exhibit obvious knee frequency. The nearly vertical feature indicates we could use a simple RC blocking electrode, as detailed in the SI to analyze the spectra. Strikingly, the cells have very small ESRs, particularly for the 3-GPB-5 cell with a value of $40\text{m}\Omega$ cm². Φ_{120} and f_o were extracted from the Bode diagrams (Figure 2e). The 3-GPB-5 cell exhibits the largest Φ_{120} value of ~85.9° and its f_0 reaches to ~3.53 kHz. The phase angle of 3-GPB-3 cell is slightly smaller (83.2°), in consistent with the slightly lower slope of its impedance line at low frequencies in Figure 2d. The reduced phase angle for 3-GPB-3 at low frequencies might be ascribed to the exposed Fe₃C particles without fully EOG coverage. The slope of impedance magnitude at low frequencies is very close to the ideal value of -1, while it is horizontal at high frequencies. The intersection of these two lines again defines the characteristic frequency f_o , the same one when the phase angle arriving -45°. The nearly constant impedance up to 100 kHz also suggests a trivial parasitic inductance, and our cells show capacitive behavior up to ~ 100 kHz where the phase angle approaches to 0. Based on analysis of complex capacitance,

the imaginary component C'' arrives its resonant maximum also at the characteristic frequency f_o (Eq. (17) in the SI), as presented in Figure 2f. The derived resonant frequency of C'' is 3.01, 3.53, and 1.31 kHz for the three cells, similar to the values acquired from Figure 2e. The frequency-dependent capacitances, derived from Eq. (18), are presented in Figure 2g. 3-GPB-7 delivers the highest specific capacitance with C_A^{120} of ~1.72 mF cm⁻² among these three samples due to its larger EOG flakes. However, these larger flakes retardate its frequency response with a smaller f_o of 1.45 kHz. Other analysis on these cells are presented in Figures S8. The normalized reactive power and resistive power of the three cells as functions of frequency are compared in Figure S9. From these studies, we concluded 5-min plasma exposure is the optimized treatment process and was selected to carry out further electrode preparation studies.

For HF-EC design, an electrode with more material loading will give a higher areal capacitance, but at the sacrifice of its frequency response. To find the appropriate loading, different amount of PB cubes of 3, 4 and 5 mg, were coated on SS disks and treated by the plasma for 5 min. The obtained samples were referred as 3-GPB-5, 4-GPB-5, and 5-GPB-5, respectively. Cross-sectional SEM images of these three samples are shown in Figure S10, from which the thickness of the active layer on SS substrate can be visually estimated. The values of mass, thickness, and volume of the GPB with different loadings are summarized in Table S1. The corresponding three cells based on these electrodes were comparatively investigated.

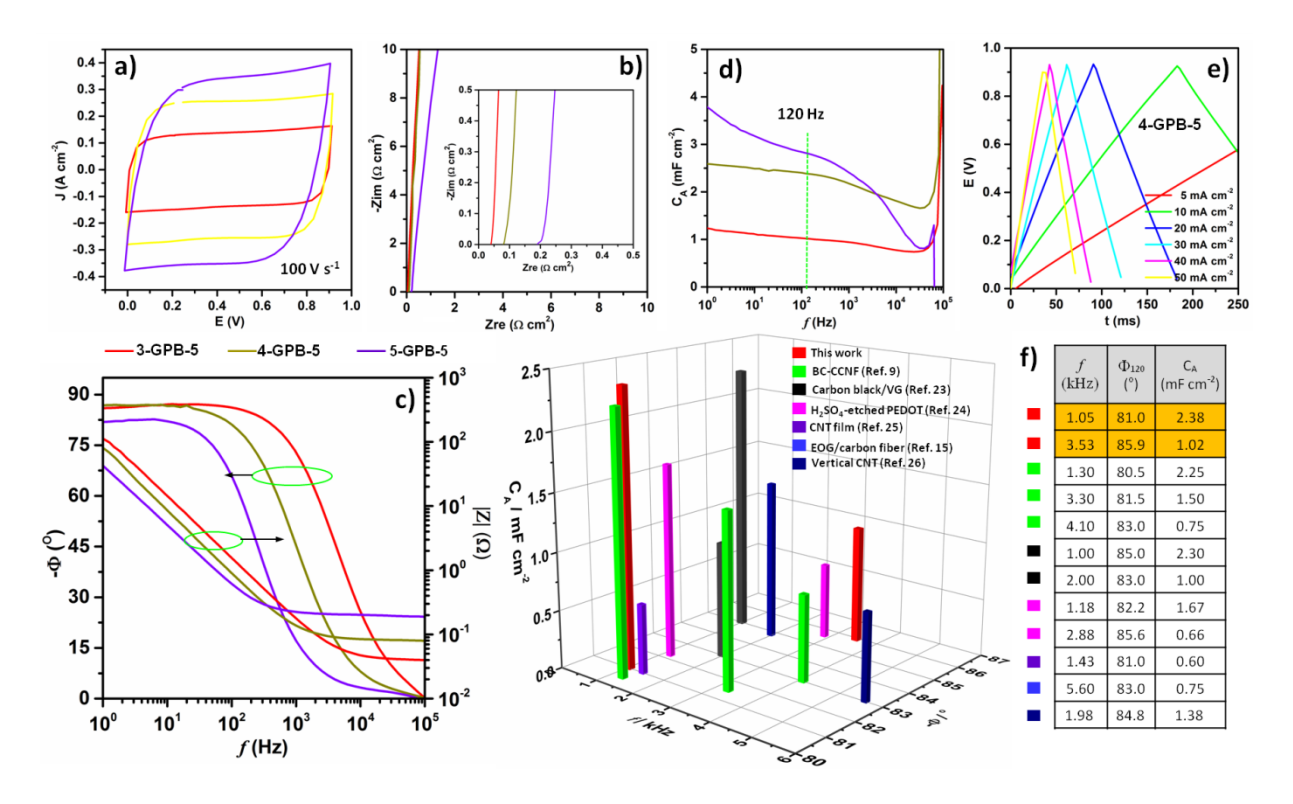


Figure 3. Electrochemical characterizations of the cells based on three samples (3-GPB-5, 4-GPB-5, and 5-GPB-5) with different material loadings: (a) CV curves recorded at 100 V s⁻¹, (b) complex-plane-impedance plots with inset displaying the high-frequency region, (c) Bode diagrams of the impedances, and (d) the derived specific capacitance versus frequency. (e) GCD curves at different current densities for a cell based on sample 4-GPB-5. (f) 3-D bar plot of results from this work in term of C_A^{120} vs. f_0 and Φ_{120} , in comparison with best results (C_A^{120} > 0.5 mF cm⁻², f_0 > 1 kHz, Φ^{120} > 80°) from the literature with symmetric sandwich-type device configuration[9, 15, 23-26] (for the electrolyte, 6 M KOH was used in ref. 9, 23, 15, 26 and this work, 1 M H₂SO₄ was used in ref. 24 and 0.5 M H₂SO₄ was used in ref. 25). These data are also tableted.

In the high-speed cyclic voltammetry (CV) measurements, all the cells exhibit a quasirectangular CV profile, as shown by the explementary curves acquired at a scan rate of 100 V s⁻¹

(Figure 3a), suggesting the ultrafast electron transport in the electrode and the minimal distributed charge storage on the electrode for rapid EDL formation[24, 25]. Their EIS spectra have similar profiles, but their ESR does increase with the loading (Figure 3b). The three cells, 3-GPB-5, 4-GPB-5, and 5-GPB-5 have a measured ESR of 40, 81 and 179 m Ω cm², respectively. In addition to the ESR contribution from the electrode material itself, a thicker layer may also prevent plasma species from deep penetration to the current collector interface, resulting in higher interfacial resistance. Bode diagrams (Figure 3c) reveal the influence of the amount of electrode materials on the cell's frequency response. Φ_{120} drops significantly from 85.9° to 62.1° with f_o decreasing from 3.53 to 0.25 kHz accordingly. The 4-GPB-5 cell still maintains Φ_{120} of 80.6° and f_0 above 1 kHz, which is capable of being used in the HF-ECs. In addition, this cell also delivers applaudable specific cell capacitance of ~2.34 mF cm⁻² at 120 Hz which only slightly decreased to ~2.0 mF cm⁻² at 1 kHz. Their specific capacitances were also calculated using the integrated area enclosed by the CV curves based on Eq.(28) in the SI, giving 1.45, 2.50 and 3.49 mF cm⁻² for 3-GPB-5, 4-GPB-5 and 5-GPB-5 cell at the scan rate of 100 V s⁻¹, respectively. The linear relationship between the scan rate and peak current (Figure S11) suggests that the cell performance is dominated by the ion absorption process, and this feature can be maintained with the scan speed up to 500 V s⁻¹ or even higher [46, 47].

For the overall best 4-GPB-5 cell, galvanostatic charge-discharge test (GCD) was carried out to further evaluate its rate capability up to 50 mA cm⁻², as presented in Figure 3e. The absence of an observable resistance-caused potential drop (IR drop) even at the current density of 50 mA cm⁻² confirms the very low ESR in the cell[6, 48]. Based on the capacitances calculated by GCD under different charge-discharge current densities, the dependence of areal and volumetric capacitance and the Ragone plot describing volumetric energy density versus power density are

presented in Figure S13. In comparison with other electrochemical devices, including thin film lithium ion battery, supercapacitor, EDLC and AEC[49-51], the GPB derived HF-EC shows much better volumetric energy density than the commercial AECs, and better power density than other devices.

The performance of these cells was further analyzed in Figure S14, including their phase angle and dissipation factor (DF) as functions of frequency, admittance-plane representation, and the real and imaginary parts of the complex capacitance as functions of frequency, and in Figure S15 for the normalized reactive power |Q|/S and the normalized power P/S as functions of frequency. The performance of the three cells is also summarized in Table 1. The long-term cycling stability tested is presented in Figure S16.

To put in a context, we compare our HF-EC with those reported in the literature with high performance in term of three most crucial parameters for line-frequency filtering: Φ_{120} , C_A^{120} , and f_0 (Figure 3f). The selection criteria are $\Phi_{120} > 80^{\circ}$, $f_0 > 1$ kHz, and $C_A^{120} > 0$. 5 mF cm⁻². Our HF-ECs using PB MOF-derived vertical graphene structures as electrodes offer one of the overall best performances.

Based on the aforementioned results, the merits of the EGO/Fe₃C electrode for high-performance HF-ECs can be summarized as following. Different from a flat metal foil surface, PB cubes act as building blocks forming a 3D architecture with widely opening pores, which significantly increases available surface area for graphene growth in the subsequent step; the rapid plasma conversion ensures the PB-derived carbon material to be free of micro-, dead- and tortuous pores and create the condition for EOG growth; the carbon layers formed outside the Fe₃C nanoparticles provide a protective shell which makes them more stable even in the corrosive electrolyte; EOG possesses excellent electron conductivity and straightforward ion

diffusion channels which guarantee their fast frequency response when used in HF-ECs; the large pores between the cube blocks prevent the usually observed porous phenomenon in a 3D structure; the *in-situ* carbonization of PB and the growth of EOG fuses the active material and current collector, eliminating the interfacial resistance which could otherwise degrade the frequency response tremendously.

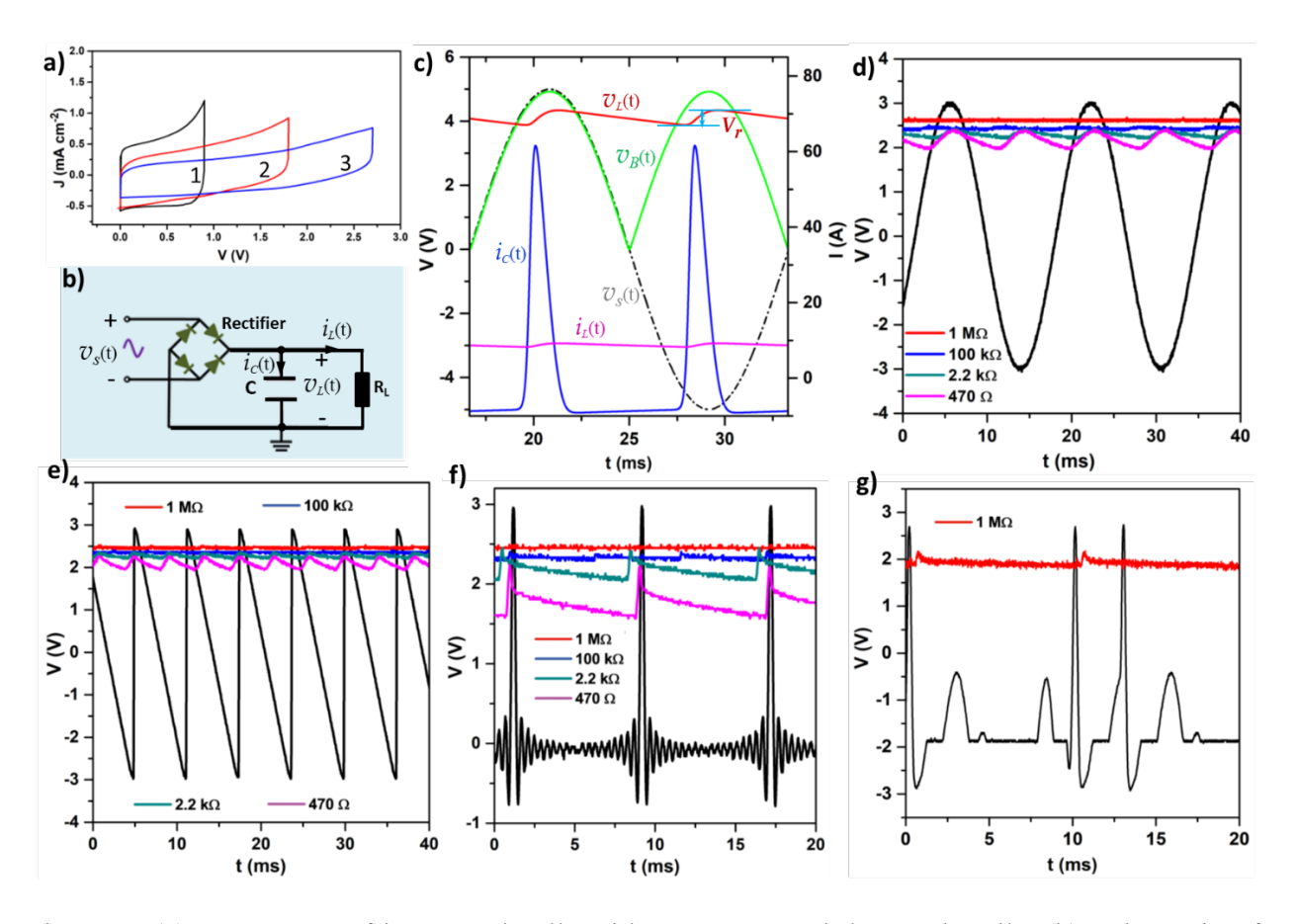


Figure 4. (a) CV curves of integrated cells with one, two, and three sub-cells. (b) Schematic of the full-wave AC/DC converter and (c) simulated voltage and current waves for 5V 60 Hz AC input. The experimentally measured output DC waves for the AC/DC converter in (b) at four different loads when the input is (d) sine, (e) triangular, (f) sinc, and (g) electro-cardio wave.

Due to the restriction of aqueous electrolytes, the stable voltage of these cells is limited to \sim 0.9 V. As a proof of concept to achieve higher voltage operation for practical applications, an integrated cell was assembled by packing three subunits together, thus extending a stable working voltage to 2.7 V (Figure 4a). Here the integrated cell was fabricated with the active material coated on nickel foil as electrodes and sealed into flat pack. Using such a high-density HF-EC, we demonstrated its function as a filtering capacitor used in an AC/DC conversion circuit (Figure 4b). One of the most crucial parameters of the AC/DC converter is the ripple voltage $V_{\rm r}$ on a given load R_L . The process of AC/DC conversion with a full-bridge rectifier and a filtering capacitor C is explained in the SI. Figure 4c shows waves simulated using PSpice assuming 60 Hz sinusoidal input with a peak value $V_{\rm m} = 5$ V, C = 0.1 mF, and $R_L = 0.47$ k Ω . The ripple voltage is approximated by

$$V_r \cong \frac{I_L T}{2C} = \frac{V_L T}{2R_L C}$$

where T is the sinusoidal AC period, I_L and V_L are the average load current and voltage, respectively. Clearly, when claiming a small ripple voltage from a filtering capacitor, the corresponding load current, or the load resistance at the given voltage must be specified.

Figure 4d presents the output of the AC/DC converter when one 2.7 V/0.1 mF HF-EC was tested as the filtering capacitor. The ripple voltage is trivial at a load resistance of 1 M Ω , and it increases to ~ 0.4 V for a 470 Ω load at an average load voltage of ~ 2.2 V. In addition to the sinusoidal wave, Figure 4e-g and S17 further confirm the filtering function of HF-EC for other AC waves, such as triangular, sinc, and electro-cardio waves. It deserves to emphasize that the pulse waves from environmental noises or vibrations can be harvested and then be stored in a compact HF-EC to drive micropower sensors in a continuous mode or milli-power devices in a

pulse mode[9]. These proof-of-concept demonstrations suggest that the reported GPB-based electrodes are promising for fabricating practical HF-ECs with excellent filtering function.

Conclusion

By employing PB cubes precursor with 3D structure to create abundant surface for graphene growth, well connected EOG architecture that has a minimized electrode resistance and straightforward pore structure was easily obtained in a one-step rapid plasma carbonization/deposition process. Due to the favorable electrode structure and the low ESR, EDL can be formed around this EOG/Fe₃C based electrodes with an extremely fast rate, thus achieving the kHz high frequency response while maintaining a reasonably large areal specific capacitance density. These have been clearly proved by the outstanding electrochemical performance that includes the absolute phase angle Φ_{120} above 80°, characteristic frequency f_0 at phase angle -45° in kHz range and 120 Hz capacitance density C_A^{120} above 2 mF cm⁻², which makes them among one of the best-reported electrode structures for HF-ECs with AC-line filtering function. Besides the reported PB cubes precursor, other MOFs or materials with regular structures are also expected to be employed as the template to produce similar 3D EOG architecture for compact HF-EC development, toward the goal of substituting the bulky AECs.

Declaration of interests

The authors declare the following financial interests/personal relationships which may be considered as potential competing interests: Z.F is a cofounder of BaoNano, LLC.

Data availability

All data generated or analyzed during the work are included in this article and its supplementary information. And the data that support our findings are available from the corresponding authors.

Acknowledgement

This work was supported by National Science Foundation (1611060).

References

- [1] J.R. Miller, R.A. Outlaw, B.C. Holloway, Graphene Double-Layer Capacitor with ac Line-Filtering Performance, Science 329 (2010) 1637-1639.
- [2] Z.Y. Fan, N. Islam, S.B. Bayne, Towards kilohertz electrochemical capacitors for filtering and pulse energy harvesting, Nano Energy 39 (2017) 306-320.
- [3] K. Sheng, Y. Sun, C. Li, W. Yuan, G. Shi, Ultrahigh-rate supercapacitors based on eletrochemically reduced graphene oxide for ac line-filtering, Sci Rep 2 (2012) 247.
- [4] G.F. Ren, X. Pan, S. Bayne, Z.Y. Fan, Kilohertz ultrafast electrochemical supercapacitors based on perpendicularly-oriented graphene grown inside of nickel foam, Carbon 71 (2014) 94-101.
- [5] Q. Jiang, N. Kurra, K. Maleski, Y.J. Lei, H.F. Liang, Y.Z. Zhang, Y. Gogotsi, H.N. Alshareef, On-Chip MXene Microsupercapacitors for AC-Line Filtering Applications, Adv. Energy Mater. 9 (2019) 9.
- [6] G.S. Gund, J.H. Park, R. Harpalsinh, M. Kota, J.H. Shin, T.I. Kim, Y. Gogotsi, H.S. Park, MXene/Polymer Hybrid Materials for Flexible AC-Filtering Electrochemical Capacitors, Joule 3 (2019) 164-176.

- [7] D. Zhao, K. Jiang, J. Li, X. Zhu, C. Ke, S. Han, E. Kymakis, X. Zhuang, Supercapacitors with alternating current line-filtering performance, BMC Materials 2 (2020) 3.
- [8] Y. Yoo, M.-S. Kim, J.-K. Kim, Y.S. Kim, W. Kim, Fast-response supercapacitors with graphitic ordered mesoporous carbons and carbon nanotubes for AC line filtering, Journal of Materials Chemistry A 4 (2016) 5062-5068.
- [9] N. Islam, S.Q. Li, G.F. Ren, Y.J. Zu, J. Warzywoda, S. Wang, Z.Y. Fan, High-frequency electrochemical capacitors based on plasma pyrolyzed bacterial cellulose aerogel for current ripple filtering and pulse energy storage, Nano Energy 40 (2017) 107-114.
- [10] M.M. Wu, F.Y. Chi, H.Y. Geng, H.Y. Ma, M. Zhang, T.T. Gao, C. Li, L.T. Qu, Arbitrary waveform AC line filtering applicable to hundreds of volts based on aqueous electrochemical capacitors, Nat. Commun. 10 (2019) 9.
- [11] S.X. Xu, W. Liu, B.M. Hu, X.H. Wang, Circuit-integratable high-frequency micro supercapacitors with filter/oscillator demonstrations, Nano Energy 58 (2019) 803-810.
- [12] M.Z. Cai, R.A. Outlaw, R.A. Quinlan, D. Premathilake, S.M. Butler, J.R. Miller, Fast Response, Vertically Oriented Graphene Nanosheet Electric Double Layer Capacitors Synthesized from C2H2, ACS Nano 8 (2014) 5873-5882.
- [13] J.R. Miller, R.A. Outlaw, Vertically-Oriented Graphene Electric Double Layer Capacitor Designs, J. Electrochem. Soc. 162 (2015) A5077-A5082.
- [14] F.Y. Chi, C. Li, Q.Q. Zhou, M. Zhang, J. Chen, X.W. Yu, G.Q. Shi, Graphene-Based Organic Electrochemical Capacitors for AC Line Filtering, Adv. Energy Mater. 7 (2017) 7.
- [15] G.F. Ren, S.Q. Li, Z.X. Fan, M.N.F. Hogue, Z.Y. Fan, Ultrahigh-rate supercapacitors with large capacitance based on edge oriented graphene coated carbonized cellulous paper as flexible freestanding electrodes, J. Power Sources 325 (2016) 152-160.

- [16] W.Y. Li, N. Islam, G.F. Ren, S.Q. Li, Z.Y. Fan, AC-Filtering Supercapacitors Based on Edge Oriented Vertical Graphene and Cross-Linked Carbon Nanofiber, Materials 12 (2019) 15.
- [17] Z. Bo, C. Xu, H. Yang, H. Shi, J. Yan, K. Cen, K. Ostrikov, Hierarchical, Vertically-Oriented Carbon Nanowall Foam Supercapacitor using Room Temperature Ionic Liquid Mixture for AC Line Filtering with Ultrahigh Energy Density, ChemElectroChem 6 (2019) 2167-2173.
- [18] Z. Bo, Z. Wen, H. Kim, G. Lu, K. Yu, J. Chen, One-step fabrication and capacitive behavior of electrochemical double layer capacitor electrodes using vertically-oriented graphene directly grown on metal, Carbon 50 (2012) 4379-4387.
- [19] J. Lin, C. Zhang, Z. Yan, Y. Zhu, Z. Peng, R.H. Hauge, D. Natelson, J.M. Tour, 3-Dimensional graphene carbon nanotube carpet-based microsupercapacitors with high electrochemical performance, Nano Lett 13 (2013) 72-78.
- [20] N. Islam, J. Warzywoda, Z. Fan, Edge-Oriented Graphene on Carbon Nanofiber for High-Frequency Supercapacitors, Nano-Micro Letters 10 (2018) 9.
- [21] M. Zhang, Q. Zhou, J. Chen, X. Yu, L. Huang, Y. Li, C. Li, G. Shi, An ultrahigh-rate electrochemical capacitor based on solution-processed highly conductive PEDOT: PSS films for AC line-filtering, Energy & Environmental Science 9 (2016) 2005-2010.
- [22] Q. Zhou, M. Zhang, J. Chen, J.D. Hong, G. Shi, Nitrogen-Doped Holey Graphene Film-Based Ultrafast Electrochemical Capacitors, ACS Appl Mater Interfaces 8 (2016) 20741-20747.
- [23] D. Premathilake, R.A. Outlaw, R.A. Quinlan, S.G. Parler, S.M. Butler, J.R. Miller, Fast Response, Carbon-Black-Coated, Vertically-Oriented Graphene Electric Double Layer Capacitors, J. Electrochem. Soc. 165 (2018) A924-A931.

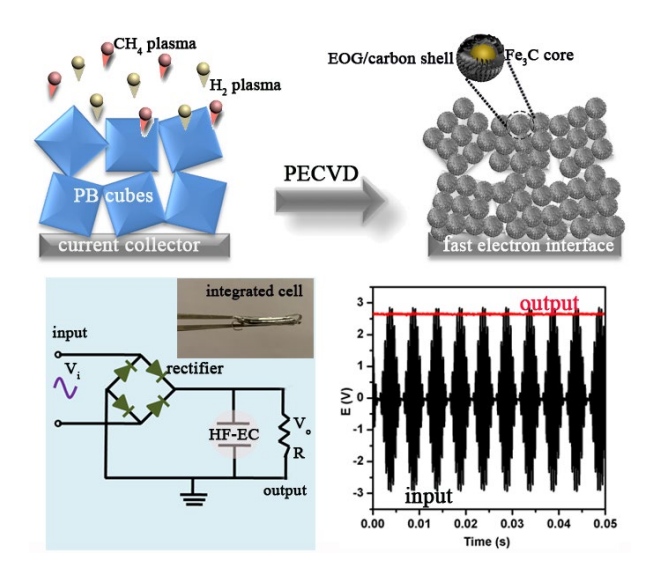
- [24] M. Zhang, Q.Q. Zhou, J. Chen, X.W. Yu, L. Huang, Y.R. Li, C. Li, G.Q. Shi, An ultrahigh-rate electrochemical capacitor based on solution-processed highly conductive PEDOT:PSS films for AC line-filtering, Energy & Environmental Science 9 (2016) 2005-2010.
- [25] Y. Rangom, X. Tang, L.F. Nazar, Carbon Nanotube-Based Supercapacitors with Excellent ac Line Filtering and Rate Capability via Improved Interfacial Impedance, ACS Nano 9 (2015) 7248-7255.
- [26] Q. Li, S.X. Sun, A.D. Smith, P. Lundgren, Y.F. Fu, P. Su, T. Xu, L.L. Ye, L.T. Sun, J. Liu, P. Enoksson, Compact and low loss electrochemical capacitors using a graphite/carbon nanotube hybrid material for miniaturized systems, J. Power Sources 412 (2019) 374-383.
- [27] C. Chen, J. Cao, X.Y. Wang, Q.Q. Lu, M.M. Han, Q.R. Wang, H.T. Dai, Z.Q. Niu, J. Chen, S.S. Xie, Highly stretchable integrated system for micro-supercapacitor with AC line filtering and UV detector, Nano Energy 42 (2017) 187-194.
- [28] Y. Yoo, S. Kim, B. Kim, W. Kim, 2.5 V compact supercapacitors based on ultrathin carbon nanotube films for AC line filtering, J. Mater. Chem. A 3 (2015) 11801-11806.
- [29] Z.Y. Zhang, M.L. Liu, X. Tian, P. Xu, C.Y. Fu, S. Wang, Y.Q. Liu, Scalable fabrication of ultrathin free-standing graphene nanomesh films for flexible ultrafast electrochemical capacitors with AC line-filtering performance, Nano Energy 50 (2018) 182-191.
- [30] N. Ji, J. Park, W. Kim, CMK-5-Based High Energy Density Electrical Double Layer Capacitor for AC Line Filtering, ACS omega 4 (2019) 18900-18907.
- [31] A. Sellam, R.N. Jenjeti, S. Sampath, Ultrahigh-Rate Supercapacitors Based on 2-Dimensional, 1T MoS2xSe2(1-x) for AC Line-Filtering Applications, J. Phys. Chem. C 122 (2018) 14186-14194.

- [32] Y. Bu, H. Liang, K. Gao, B. Zhang, X. Zhang, X. Shen, H. Li, J. Zhang, Wafer-scale fabrication of high-purity reduced graphene oxide films as ultrahigh-frequency capacitors with minimal self-discharge, Chemical Engineering Journal (2020) 124560.
- [33] M. Zhao, J. Nie, H. Li, M. Xia, M. Liu, Z. Zhang, X. Liang, R. Qi, Z.L. Wang, X. Lu, High-frequency supercapacitors based on carbonized melamine foam as energy storage devices for triboelectric nanogenerators, Nano Energy 55 (2019) 447-453.
- [34] B.Y. Guan, X.Y. Yu, H.B. Wu, X.W. Lou, Complex Nanostructures from Materials based on Metal-Organic Frameworks for Electrochemical Energy Storage and Conversion, Adv. Mater. 29 (2017) 20.
- [35] G.Q. Zou, H.S. Hou, P. Ge, Z.D. Huang, G.G. Zhao, D.L. Yin, X.B. Ji, Metal-Organic Framework-Derived Materials for Sodium Energy Storage, Small 14 (2018) 27.
- [36] H.L. Jiang, B. Liu, Y.Q. Lan, K. Kuratani, T. Akita, H. Shioyama, F.Q. Zong, Q. Xu, From Metal-Organic Framework to Nanoporous Carbon: Toward a Very High Surface Area and Hydrogen Uptake, J. Am. Chem. Soc. 133 (2011) 11854-11857.
- [37] W.Y. Li, N. Islam, S. Azam, Z. Xu, J. Warzywoda, Z.Y. Fan, ZIF-67-derived edge-oriented graphene clusters coupled with carbon nanotubes containing encapsulated Co nanoparticles for high-frequency electrochemical capacitors, Sustainable Energy & Fuels 3 (2019) 3029-3037.
- [38] X. Yang, Y.B. Tang, X. Huang, H.T. Xue, W.P. Kang, W.Y. Li, T.W. Ng, C.S. Lee, Lithium ion battery application of porous composite oxide microcubes prepared via metalorganic frameworks, J. Power Sources 284 (2015) 109-114.
- [39] N. Islam, M.N.F. Hoque, W. Li, S. Wang, J. Warzywoda, Z. Fan, Vertically edge-oriented graphene on plasma pyrolyzed cellulose fibers and demonstration of kilohertz high-frequency filtering electrical double layer capacitors, Carbon 141 (2019) 523-530.

- [40] E. Dervishi, Z.R. Li, F. Watanabe, A. Biswas, Y. Xu, A.R. Biris, V. Saini, A.S. Biris, Large-scale graphene production by RF-cCVD method, Chem. Commun. (2009) 4061-4063.
- [41] A. Kraupner, M. Antonietti, R. Palkovits, K. Schlicht, C. Giordano, Mesoporous Fe3C sponges as magnetic supports and as heterogeneous catalyst, J. Mater. Chem. 20 (2010) 6019-6022.
- [42] L.M. Malard, M.A. Pimenta, G. Dresselhaus, M.S. Dresselhaus, Raman spectroscopy in graphene, Phys. Rep.-Rev. Sec. Phys. Lett. 473 (2009) 51-87.
- [43] N. Wang, W. Ma, Z. Ren, Y. Du, P. Xu, X. Han, Prussian blue analogues derived porous nitrogen-doped carbon microspheres as high-performance metal-free peroxymonosulfate activators for non-radical-dominated degradation of organic pollutants, Journal of Materials Chemistry A 6 (2018) 884-895.
- [44] C. Xuan, J. Wang, W. Xia, Z. Peng, Z. Wu, W. Lei, K. Xia, H.L. Xin, D. Wang, Porous structured Ni–Fe–P nanocubes derived from a prussian blue analogue as an electrocatalyst for efficient overall water splitting, ACS applied materials & interfaces 9 (2017) 26134-26142.
- [45] N.P. Wickramaratne, V.S. Perera, B.-W. Park, M. Gao, G.W. McGimpsey, S.D. Huang, M. Jaroniec, Graphitic mesoporous carbons with embedded prussian blue-derived iron oxide nanoparticles synthesized by soft templating and low-temperature graphitization, Chemistry of Materials 25 (2013) 2803-2811.
- [46] S.M. Mirvakili, I.W. Hunter, Vertically Aligned Niobium Nanowire Arrays for Fast-Charging Micro-Supercapacitors, Adv. Mater. 29 (2017) 6.
- [47] D. Pech, M. Brunet, H. Durou, P.H. Huang, V. Mochalin, Y. Gogotsi, P.L. Taberna, P. Simon, Ultrahigh-power micrometre-sized supercapacitors based on onion-like carbon, Nat. Nanotechnol. 5 (2010) 651-654.

- [48] Y.L. Shao, J.M. Li, Y.G. Li, H.Z. Wang, Q.H. Zhang, R.B. Kaner, Flexible quasi-solid-state planar micro-supercapacitor based on cellular graphene films, Mater. Horizons 4 (2017) 1145-1150.
- [49] J. Lin, Z.W. Peng, Y.Y. Liu, F. Ruiz-Zepeda, R.Q. Ye, E.L.G. Samuel, M.J. Yacaman, B.I. Yakobson, J.M. Tour, Laser-induced porous graphene films from commercial polymers, Nat. Commun. 5 (2014) 8.
- [50] W.L. Zhang, Y.J. Lei, Q. Jiang, F.W. Ming, P. Costa, H.N. Aishareef, 3D Laser Scribed Graphene Derived from Carbon Nanospheres: An Ultrahigh-Power Electrode for Supercapacitors, Small Methods 3 (2019) 8.
- [51] V. Strauss, K. Marsh, M.D. Kowal, M. El-Kady, R.B. Kaner, A Simple Route to Porous Graphene from Carbon Nanodots for Supercapacitor Applications, Adv. Mater. 30 (2018) 10.

Table of Content (ToC)



Supplementary Materials

Prussian Blue Based Vertical Graphene 3D Structure for High Frequency Electrochemical Capacitor

Wenyue Li, Sakibul Azam, Guangzhen Dai, Zhaoyang Fan*

Department of Electrical and Computer Engineering and Nano Tech Center, Texas Tech University, Lubbock, TX, 79409, USA

*Corresponding author: zhaoyang.fan@ttu.edu

Contents:

1. EIS Spectrum Analysis		
1.1 The ideal blocking electrode	2	
1.2 The experimental electrodes	5	
2. Experimental Section	8	
2.1 Materials synthesis and characterization	8	
2.2 Electrochemical measurements	9	
3. Supplemental Data		
4. AC/DC Conversion and Ripple Voltage		
4.1 General process in AC/DC conversion	24	
4.2 Low voltage AC/DC conversion	26	

1. EIS Spectrum Analysis

For kHz high frequency ECs, its impedance data, when represented in the complex-impedance-plane (Nyquist plot), approaches to a vertical line, and hence such electrodes could be approximately modeled as a simple series RC blocking electrode, or the HF-ECs as an ideal series RC component. Such an approximation is acceptable only when: 1) the Nyquist plot is close to a vertical line and 2) for frequencies up to a knee frequency (f_k), or if f_k does not exist, for frequencies where the parasitic inductance can be neglected.

1.1 The ideal blocking electrode

Some of the impedance characteristics of an ideal series RC blocking electrode (Figure S1a) are presented in Figure S1b-f, assuming $R = 50 \text{ m}\Omega \text{ cm}^2$ and $C = 1 \text{ mF cm}^{-2}$.

Its impedance Z, capacitance C, and phase Φ are given by

$$Z = Z' + jZ'' = R - j\frac{1}{\omega C} \tag{1}$$

$$C = \frac{-1}{\omega Z''} \tag{2}$$

$$\Phi = \arctan\left(\frac{Z'}{Z''}\right) = -\arctan\left(\frac{1}{\omega RC}\right)$$
(3)

$$X_C = \frac{1}{\omega C} \tag{4}$$

where $\omega = 2\pi f$ is the angular frequency, Z' is the real and Z'' is the imaginary components of the impedance, and X_C is the reactance of the capacitor.

As depicted in Figure S1a, loss tangent $\tan \delta$ is defined as

$$\tan \delta = \frac{Z'}{-Z''} = \frac{R}{X_C} = \omega RC \tag{5}$$

and the dissipation factor DF as

$$DF = \tan\delta \times 100\% \tag{6}$$

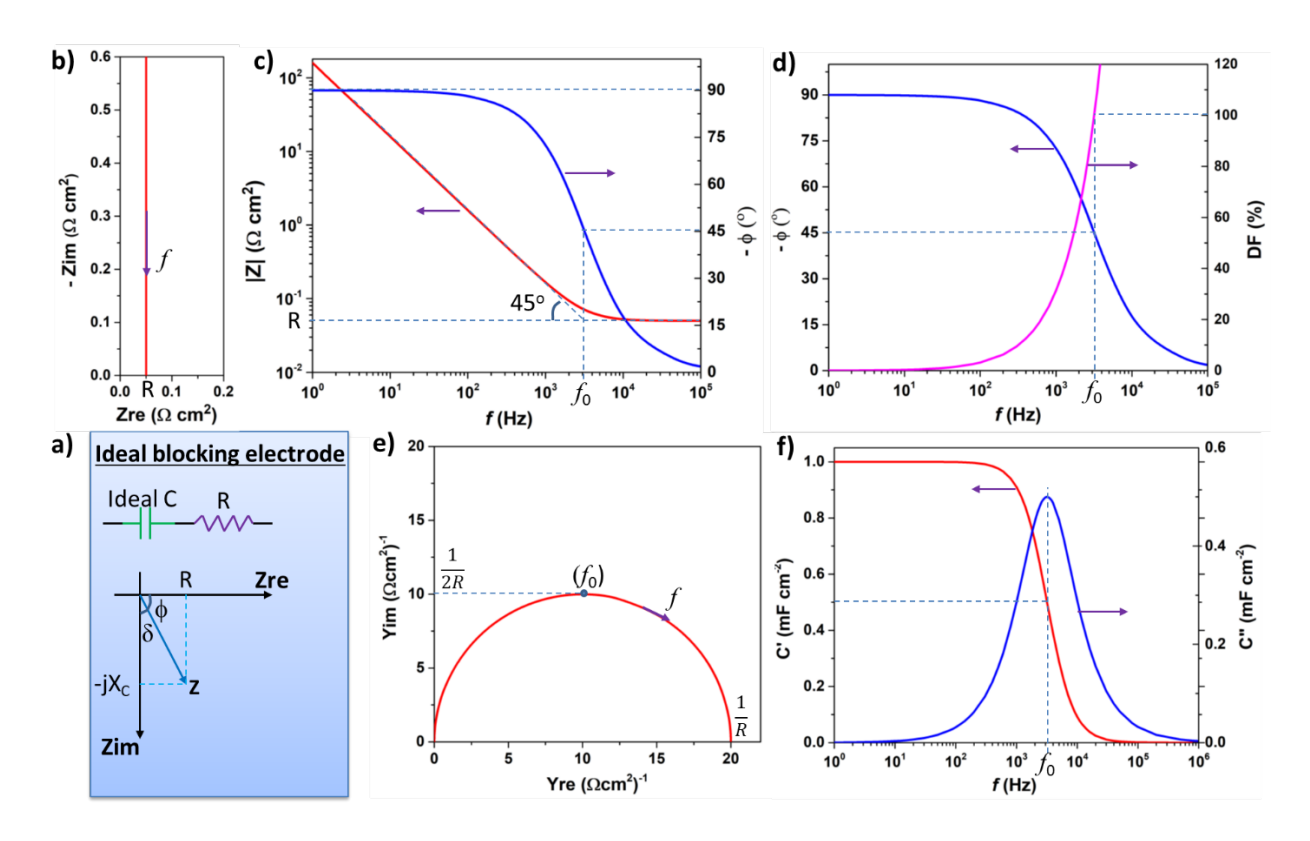


Figure S1.a) Schematic of an ideal blocking electrode and the loss tangent. Impedance spectrum represented in different formats for the ideal RC in series: b) Nyquist format, c) Bode format, d) phase angle and dissipation factor as a function of frequency, e) admittance-plane representation, and f) real and imaginary part of the complex capacitance as a function of frequency. Assuming with $R = 50 \text{ m}\Omega \text{ cm}^2$ and $C = 1 \text{ mF cm}^{-2}$.

In Figure S1b, the impedance data of the ideal blocking electrode is represented in the complex-impedance-plane or Nyquist format. The data are presented as a locus of points, where each data point corresponds to the impedance measured at a different frequency. For the blocking electrode, it is a vertical line, crossing the Zre-axis at a value of R when $\omega \to \infty$.

At the phase angle of -45° , Z' = Z'', and therefore the characteristic frequency f_0

$$f_0 = \frac{1}{2\pi RC} \tag{7}$$

The magnitude of the impedance is expressed as

$$|Z| = \sqrt{R^2 + \left(\frac{1}{\omega C}\right)^2} \tag{8}$$

In the Bode diagram of $\log |Z|vs \log f$, at low frequencies when $(2\pi fC)^{-1} \gg R$,

$$\log|Z| = -\log f - \log(2\pi\mathcal{C}) \tag{9}$$

which is a straight line with a slope of -1; at high frequencies when $(2\pi fC)^{-1} \ll R$,

$$\log|Z| = \log R \tag{10}$$

which is a horizontal line. The extrapolation of these two lines intersect at $f_0 = (2\pi RC)^{-1}$.

All these features can be noticed in the Bode plot (Figure S1c). Figure S1d further presents the phase angle and the dissipation factor with respect to frequency. At f_0 , DF = 100% since $X_C = R$.

The impedance spectrum of the series *RC* electrode can be analyzed using its admittance format, expressed as

$$Y = \frac{1}{Z} = Y' + jY'' = \frac{R(\omega C)^2}{1 + (\omega RC)^2} + j \frac{\omega C}{1 + (\omega RC)^2}$$
(11)

which displays a semicircle on the complex-admittance-plane plot, with the center of the circle at $(\frac{1}{2R}, 0)$, as shown in Figure S1e. Y approaches zero at low frequencies, and $\frac{1}{R}$ at high frequencies. The maximum Y"value is found at the characteristic frequency f_0 to be

$$Y''_{\text{max}} = \frac{1}{2R} \tag{12}$$

The concept of a complex capacitance can be introduced for further analysis of an EC with resistive losses, which is defined to be

$$C_c(\omega) = C'(\omega) - jC''(\omega) = \frac{1}{j\omega Z} = -j\frac{Y}{\omega} = \frac{-Z'' - jZ'}{\omega|Z|^2}$$
(13)

and hence

$$C'(\omega) = \frac{-Z''}{\omega |Z|^2} = -\frac{\sin \varphi}{\omega |Z|} \tag{14}$$

$$C''(\omega) = \frac{Z'}{\omega |Z|^2} = \frac{\cos \varphi}{\omega |Z|} \tag{15}$$

where, φ is the phase angle of the impedance at the corresponding frequency.

For the blocking electrode-based ECs,

$$C'(\omega) = \frac{c}{1 + (\omega RC)^2} \tag{16}$$

$$C''(\omega) = \frac{\omega RC^2}{1 + (\omega RC)^2} \tag{17}$$

where C'' arrives its resonant maximum at the characteristic frequency f_0 . This can be noticed in Figure S1f. Also note that at this frequency, $C'(\omega_0) = \frac{C}{1 + (\omega_0 RC)^2} = \frac{C}{2}$.

1.2 The experimental electrodes

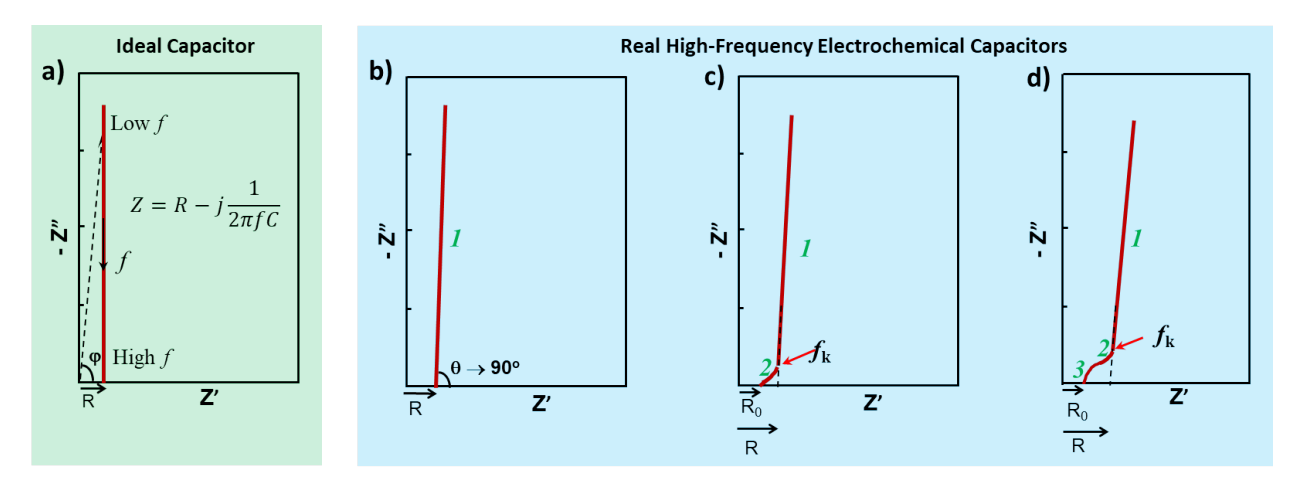


Figure S2. Schematic of impedance spectra for the ideal blocking electrode-based capacitor in (a) and for realistic HF-ECs for (b-c). Only the impedance spectra in section 1 can be approximately modeled as the ideal capacitor in (a).

The behavior of real electrodes deviates from that of the ideal blocking electrode, as

schematically depicted in Figure S2. A well-designed electrode for HF-EC should behave like that in Figure S2b, where the EIS spectrum is not a perfect vertical line, but the angle θ approaches to 90°. Therefore, instead of using a constant phase element, the EIS spectrum in Figure S2b might be modeled as the ideal capacitor in Figure S2a.

In such a case, based on equation (2), the areal specific cell capacitance of an EC can be calculated from its EIS spectra using the following equation:

$$C_A(f) = \frac{-1}{2\pi f Z^{\prime\prime} A} \tag{18}$$

Where *A* is the area of a single electrode.

However, it is difficult to completely eliminate the porous effect from the electrode, particularly if relatively thick electrodes are used to pursue a large capacitance. Therefore, the impedance spectra of most electrodes for HF-ECs still have a small tail with a 45° characteristic line at high frequency, suggesting the trace mark of porosity of the electrode, as shown in Figure S2c. It is obvious, for such electrodes, the ideal blocking electrode model can only be used to model their impedance spectra up to their knee frequency f_k , as long as the spectra are still close to a vertical line for $f < f_k$. It should also be emphasized that the ERS should be reported as R, but not R_0 .

If the electrodes are not well prepared, two other adverse phenomena may appear. For one case, a relatively large interfacial resistance, due to an interfacial resistive layer or Schottky-like contact, may exist between the electrode material and the current collector, and for the other case, a charge transfer mechanism between the electrolyte and the electrode (the pseudocapacitance effect) might exist. Either of the two situations will introduce an extra R//C circuit element in series with other elements (e.g. the ideal capacitor with an ESR) and gives rise to the semicircle trace at high frequencies, as shown in Figure S2d. For such electrodes, we might still use the

ideal blocking electrode model for the frequency range below the knee frequency f_k . And again, the ERS should be reported as R, but not R_0 .

In addition to the above blocking electrode-based capacitor model, further analysis of an EC can be conducted by introducing the complex capacitance, as defined in equations (13-15). At low frequencies, the value of $C'(\omega)$ corresponds to the capacitance of the cell measured under low constant discharge. $C''(\omega)$, the imaginary part of the capacitance $C(\omega)$, is associated with energy dissipation due to internal loss. It deserves to emphasize that $C'(\omega)$ should have a value like that derived from Eq. (18). A large difference between these two values will suggest the behavior of the tested electrode deviates far away from the ideal blocking electrode.

Treating the nonideal ECs as a load powered by a sinusoidal source $V(\omega)$, the power P, reactive power Q, and the apparent power S can be derived from the complex power S, defined as:

$$\mathbf{S} = P + jQ = \frac{1}{2}\mathbf{V}\mathbf{I}^* \tag{19}$$

where the phasor voltage $\mathbf{V} = V_m \angle \varphi_v$ with V_m being the peak value and φ_v being the phase angle of the voltage, and the phasor current $\mathbf{I} = I_m \angle \varphi_i$ with I_m being the peak value and φ_i being the phase angle of the current. The impedance

$$Z = \frac{\mathbf{V}}{\mathbf{I}} = \frac{V_m}{I_m} \angle \varphi = |Z| \angle \varphi \tag{20}$$

where, $|Z| = \frac{V_m}{I_m}$ and $\varphi = \varphi_v - \varphi_i$. Substituting into Eq. (19), we have

$$\mathbf{S} = \frac{V_m^2}{2|\mathbf{Z}|} \angle \varphi = \frac{V_m^2}{2|\mathbf{Z}|} \cos \varphi + j \frac{V_m^2}{2|\mathbf{Z}|} \sin \varphi \tag{21}$$

Hence

$$P = \frac{V_m^2}{2|\mathbf{Z}|}\cos\varphi\tag{22}$$

$$Q = \frac{V_m^2}{2|\mathbf{Z}|} \sin \varphi \tag{23}$$

$$S = \frac{V_m^2}{2|\mathbf{Z}|} \tag{24}$$

In comparison to Eqs. (14, 15), we have

$$P = \frac{V_m^2}{2} \omega C'' \tag{25}$$

$$Q = -\frac{V_m^2}{2}\omega C' \tag{26}$$

Since an EC oscillates between capacitance dominance at low frequencies and resistance dominance at high frequencies, the normalized power P/S and the normalized reactive power |Q|/S will have a value between 0 and 1. When these two normalized powers qual, φ will be 45° and the normalized power will be $\frac{1}{\sqrt{2}}$. It is further noticed that the loss tangent

$$\tan \delta = \frac{P}{|Q|} \tag{27}$$

When φ reaches 45°, DF= 100%.

2. Experimental Section

2.1 Materials synthesis and characterization

Prussian blue cubes (PB cubes) were synthesized according to previously reported method³⁵. Briefly, 0.41 g of potassium ferricyanide (K₄Fe(CN)₆·3H₂O) and 5 g of polyvinylpyrrolidone (PVP) were firstly dissolved into 100 mL of 0.1 M HCl solution under stirring at 80°C for half an hour. Then, the above solution was transferred into an oven and aged for 24 h at the same temperature. The resulted PB cubes were separated and washed with DI water and ethanol for several time by centrifuge. As for comparison, different amounts of PVP (3, 5 and 7 g) were used to obtain PB cubes with various sizes.

50 mg of PB cubes synthesized using 3 g PVP was ultrasonically dispersed into 5 mL of ethanol to get uniform precursor ink. And 300 μL of the prepared ink (total amount of PB cubes was 3 mg) was dropped onto a manually polished stainless-steel disk (SS, diameter: ~1.56 cm), and dried in an oven at 60 °C overnight. The sample was then loaded into a PECVD system. After the system was evacuated, 100 sccm of hydrogen and 50 sccm of methane were introduced and the chamber pressure was controlled at 30 Torr. At a substrate temperature of 750°C, 1 kW microwave radiation was turned on to generate plasma. This plasma process was continued for 3, 5, or 7 min, and the resulted samples were designated as 3-GPB-3, 3-GPB-5 and 3-GPB-7, respectively. Another set of electrode samples with different thicknesses were also prepared by changing the amount of the PB ink of 3, 4 and 5 mg coated on SS, which were all treated in the plasma for 5 min. These samples were referred to as 3-GPB-5, 4-GPB-5 and 5-GPB-5, respectively. Sample using the same recipe but without exposing to the plasma, referred as CPB, was also synthesized for comparison.

The morphology of all the samples was observed by using field emission scanning electron microscopy (FE-SEM, Supra35, Gemini) and transmission electron microscopy (TEM, H-8100, Hitachi). The crystalline phases of the samples were determined based on X-ray diffraction (XRD, MiniFlex 6G, Rigaku) measured with 2θ from 10° to 80° using Cu Kα radiation.

2.2 Electrochemical measurements

Symmetric coin cells (CR 2016) were assembled using these carbonized PB samples as electrodes, Celgard membrane as the separator and 6 M KOH as the electrolyte. All measurements were carried out on a Biologic electrochemical workstation. The cyclic voltammetry curves (CVs) were recorded under a variety of scan rates in the voltage range of

0.0-0.9 V and the electrochemical impedance spectroscopy (EIS) data was obtained in the frequency range from 100 KHz to 1 Hz with 10 mV AC signal. Galvanostatic charge-discharge (GCD) measurement was carried out under different current densities from 5 to 50 mA cm⁻². The stability test was performed by using the prepared coin cells under the current density of 10 mA cm⁻².

CV curves were also used to calculate the specific cell capacitance calculation and the corresponding equation is given below,

$$C_A = \frac{\int_0^{\Delta V} i d\mathbf{v}}{v(\Delta V)A} \tag{28}$$

where ν is the scan rate and ΔV is the scanned voltage range.

For the integrated cell preparation, PB-5 was coated on Ni foil and carbonized in PECVD system, the obtained EOG materials were cut into 1cm * 1cm pieces as electrodes and sealed into laminated aluminum film with separator and electrolyte. Three cell units were further connected in series by welding process.

For the AC-line filtering measurement, the circuit used is given in Figure 4b, and the input AC was supplied by an arbitrary function generator, and the output voltage on the load was recorded by a digital oscilloscope.

3. Supplemental Data

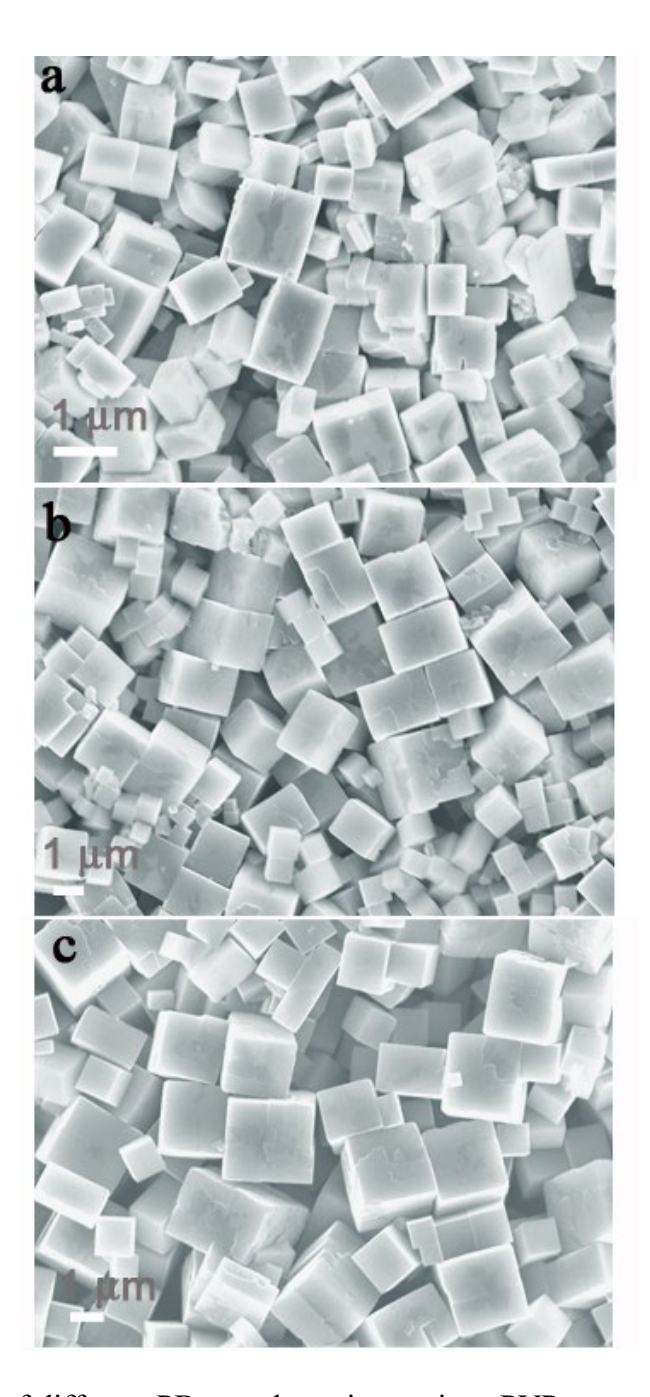


Figure S3. SEM images of different PB samples using various PVP structural modifier of 3 g in a), 5g in b) and 7 g in c). With more PVP adding into the potassium ferricyanide solution, the size of PB cubes and their uniformity increases. For example, the average size of the PB with 3 PVP is around 1 μ m, which is much smaller than that synthesized with 7 PVP (~2.5 μ m).

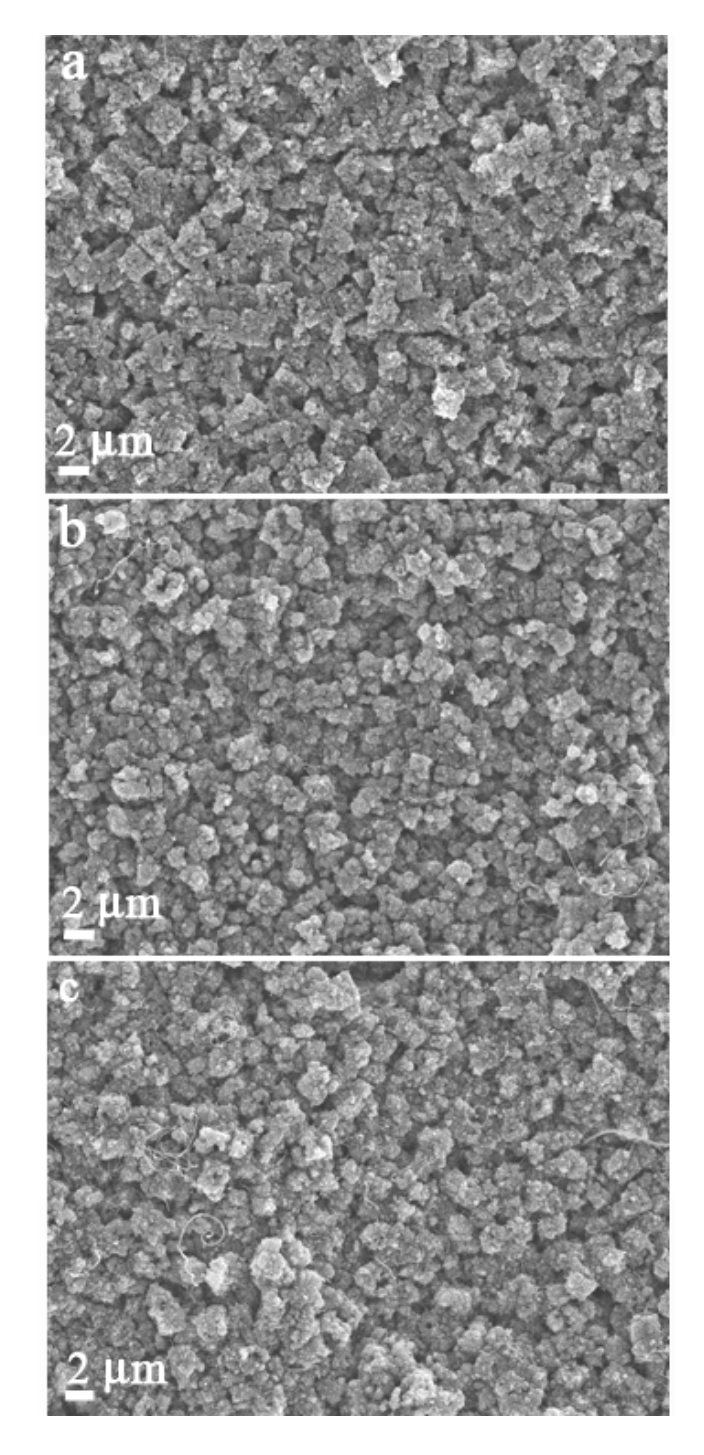


Figure S4. SEM images of 3-GPB-3, 3-GPB-5 and 3-GPB-7 samples at low magnification. These images reveal the slight shape deformation of PB cubes after carbonization and EOG growth, but the overall granular morphology was maintained.

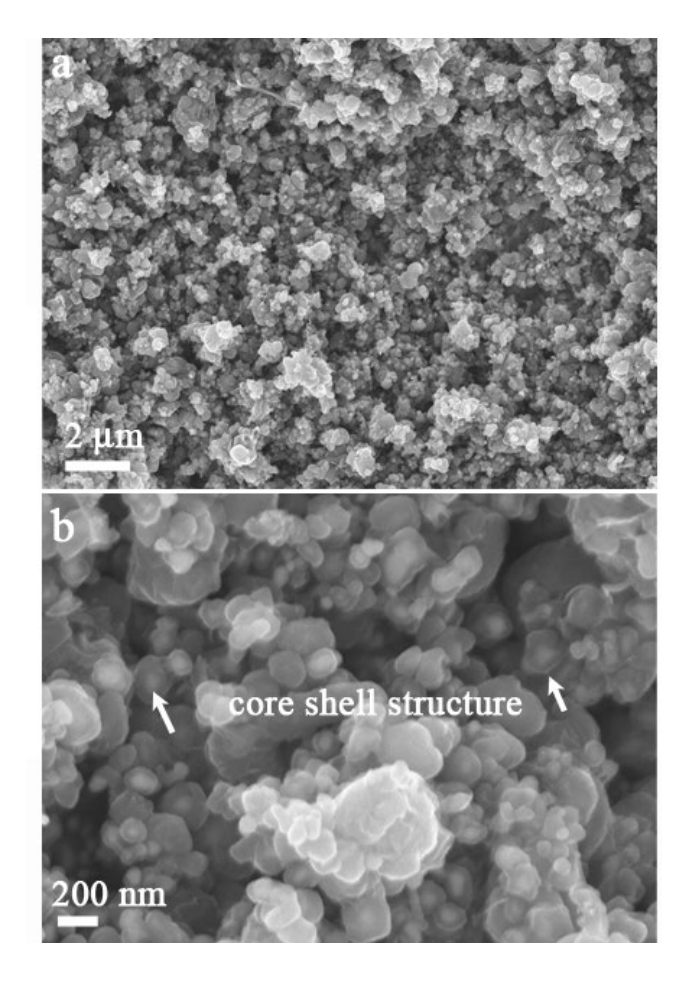


Figure S5. SEM images of carbonized PB at two different magnifications. PB cubes treated in the PECVD without exposing to plasmas also shows core-shell structure but is absent of EOG nanosheets, proving that the plasma is essential to create the EOG material.

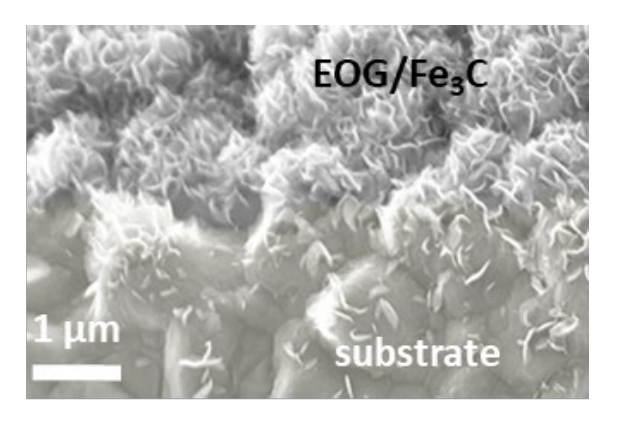


Figure S6. Cross-sectional SEM image of 3-GPB-5 electrode.

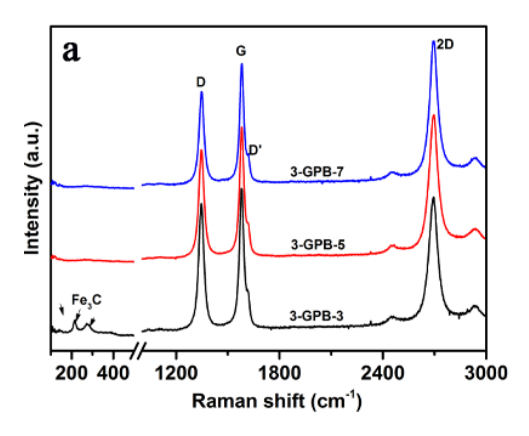


Figure S7. Raman spectra of Sample 3-GPB-3, 3-GPB-5, and 3-GPB-7.

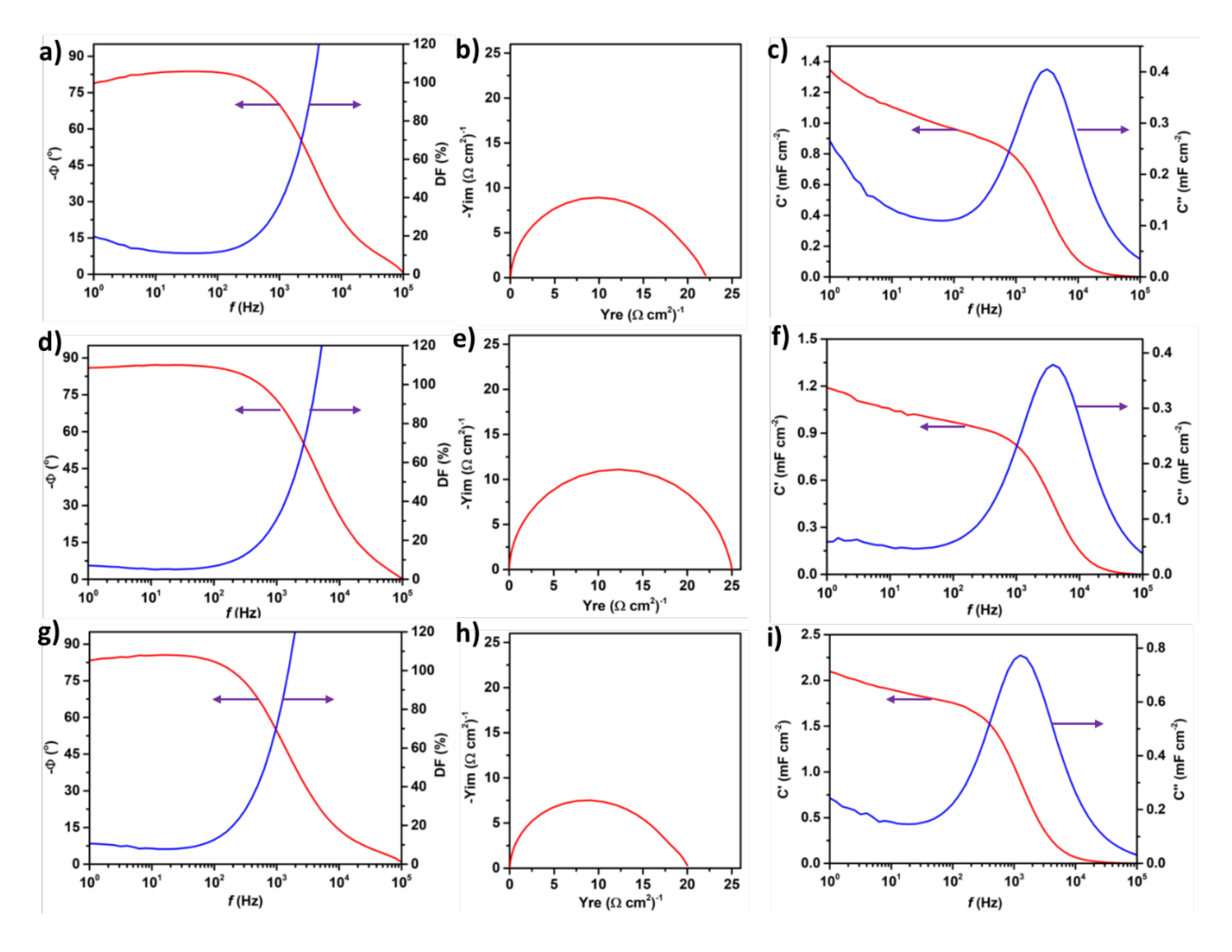


Figure S8. Phase angle and dissipation factor (DF) as functions of frequency (a, d, g), admittance-plane representation of EIS (b, e, h), and the real and imaginary parts of the complex capacitance as functions of frequency (c, f, i). (a-c) are for 3-GPB-3, (d-f) are for 3-GPB-5, and (g-i) are for 3-GPB-7 cell.

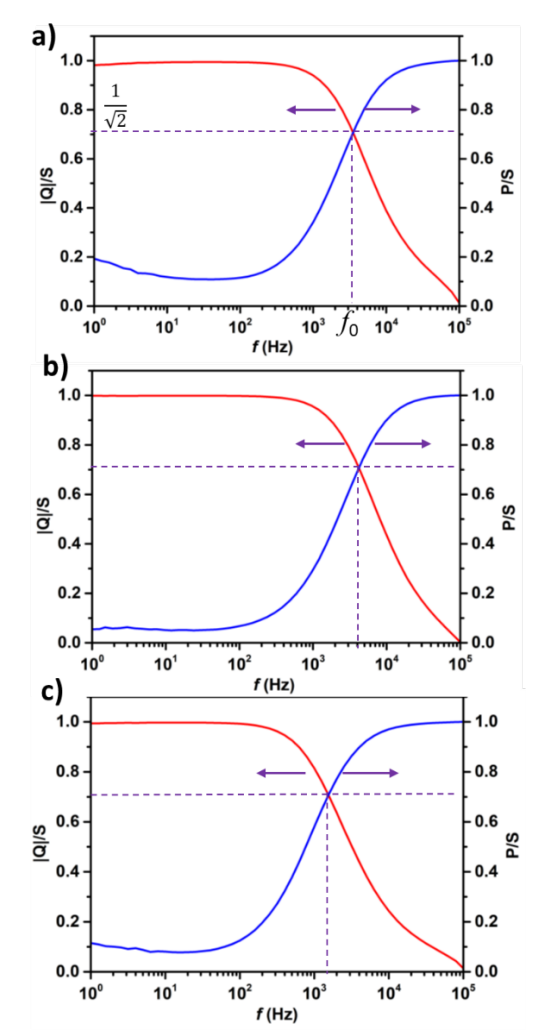


Figure S9. The normalized reactive power |Q|/S and the normalized power P/S as functions of frequency: (a) for 3-GPB-3, (b) for 3-GPB-5, and (c) for 3-GPB-7 cell.

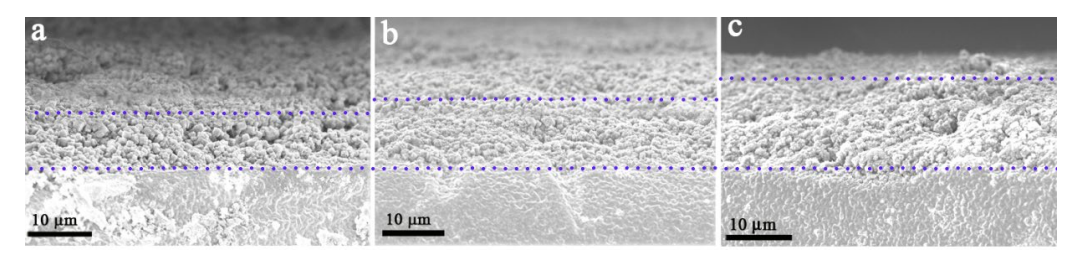


Figure S10. Cross-sectional SEM images of samples (a) 3-GPB-5, (b) 4-GPB-5 and (c) 5-GPB-5.

Table S1 Mass loading, thickness, and volume of active layers for different samples.

	m (mg)	d (µm)	$V (* 10^{-3} \text{ cm}^3)$
3-GPB-5	2.1	8.2	1.6
4-GPB-5	2.7	10.3	2.0
5-GPB-5	3.4	13.3	2.5

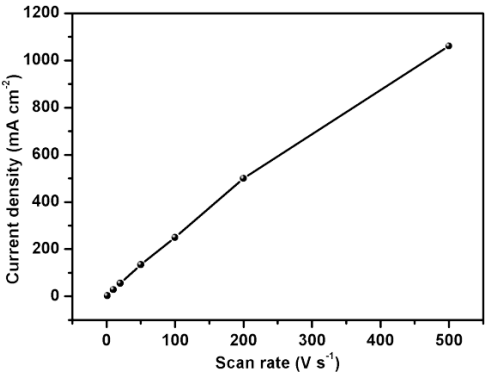


Figure S11. Plot of peak current density versus scan rate derived from CV curves for Cell 5-PB-5. The linear relationship between current density and scan rate extracted from CV curves demonstrates the excellent capacitive behavior.

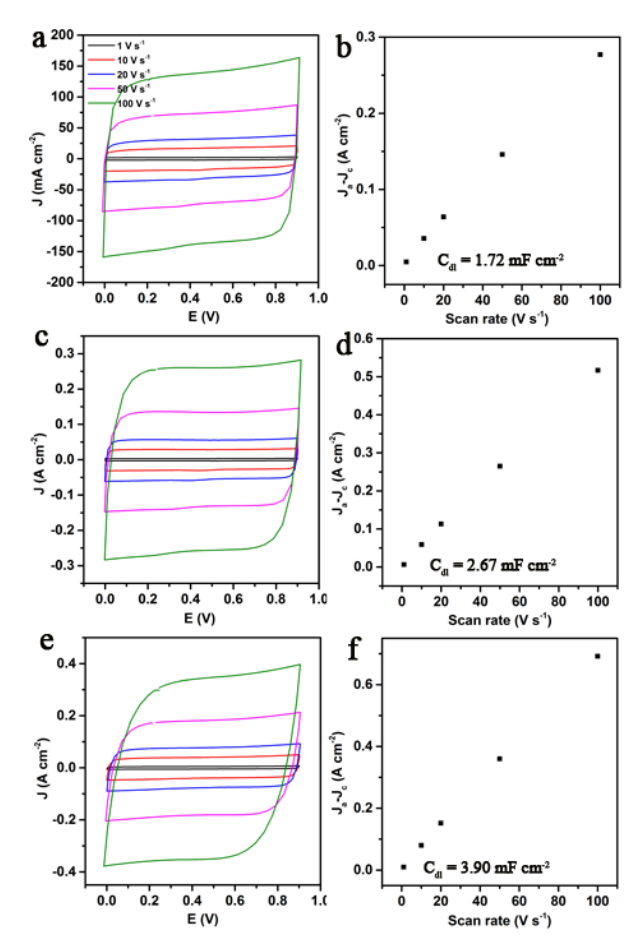


Figure S12. Cyclic voltammetry curves of cells with (a) 3-GPB-5 electrodes, (c) 4-GPB-5 electrodes and (e) 5-GPB-5 electrodes recorded at various scan rates (ν) from 1 to 100 V s⁻¹. Scan rate dependence of the current densities of (b) 3-GPB-5 electrodes and (d) 4-GPB-5 electrode and (f) 5-GPB-5 electrodes.

Electrochemical active surface area (ECSA) was estimated for the three samples: 3-GPB-5, 4-GPB-5 and 5-GPB-5, using the formula ECSA = C_{dl}/C_s , where C_{dl} is the electrochemical double layer capacitance of the electrode and Cs is the specific areal capacitance of a flat surface. Here we measured the specific capacitance of the stainless-steel spacer used in the coin cell, assuming its surface roughness being negligible, which was found to be 22.5 μ Fcm⁻². We used the CV recorded at 1, 10, 20, 50, 100 V s⁻¹ to calculate the average C_{dl} based on $C_{dl} = (J_a-J_c)/2\nu$, where J_a is anodic current density, J_c is cathodic current density and ν is the scan rate. The ECSA value for 3-GPB-5, 4-GPB-5 and 5-GPB-5 was found to be 77.4, 118.6 and 173.3 cm², respectively, much larger than their geometric surface area of 1.91 cm².

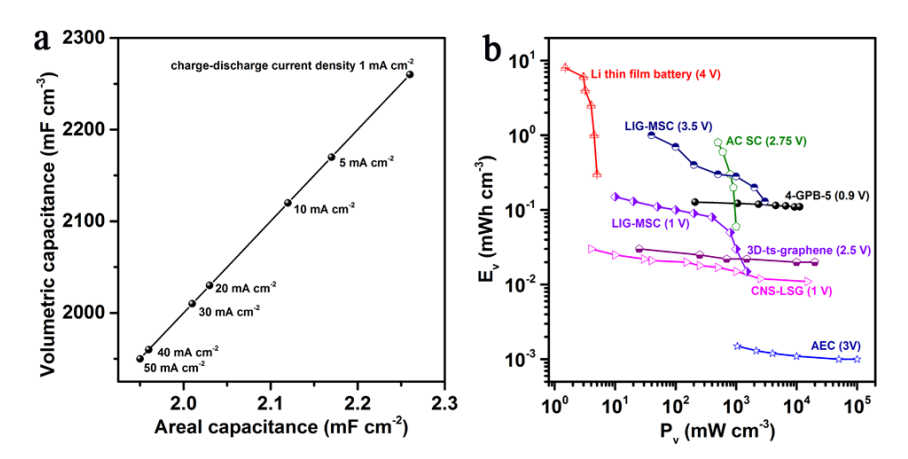


Figure S13. (a) The dependence of the areal and the volumetric capacitance. (b) The electrode volumetric Ragone plot of the 4-GPB-5 based HF-EC, in comparison to reported supercapacitor, EDLC, Li thin-film battery, and aluminum electrolytic capacitor [49-51].

The volumetric energy density (E_v) and power density (P_v) were calculated based on the following equations:

$$E_{\rm v} = \frac{1}{2} \times \frac{C_{\rm A} V^2}{3600 \times 2d} \tag{29}$$

$$P_{v} = \frac{3600 \times E_{v}}{\Delta t} \tag{30}$$

Where C_A is the areal capacitance obtained by the GCD test, V is working window of the cell, d is the thickness of the active layer, and Δt is the discharging time.

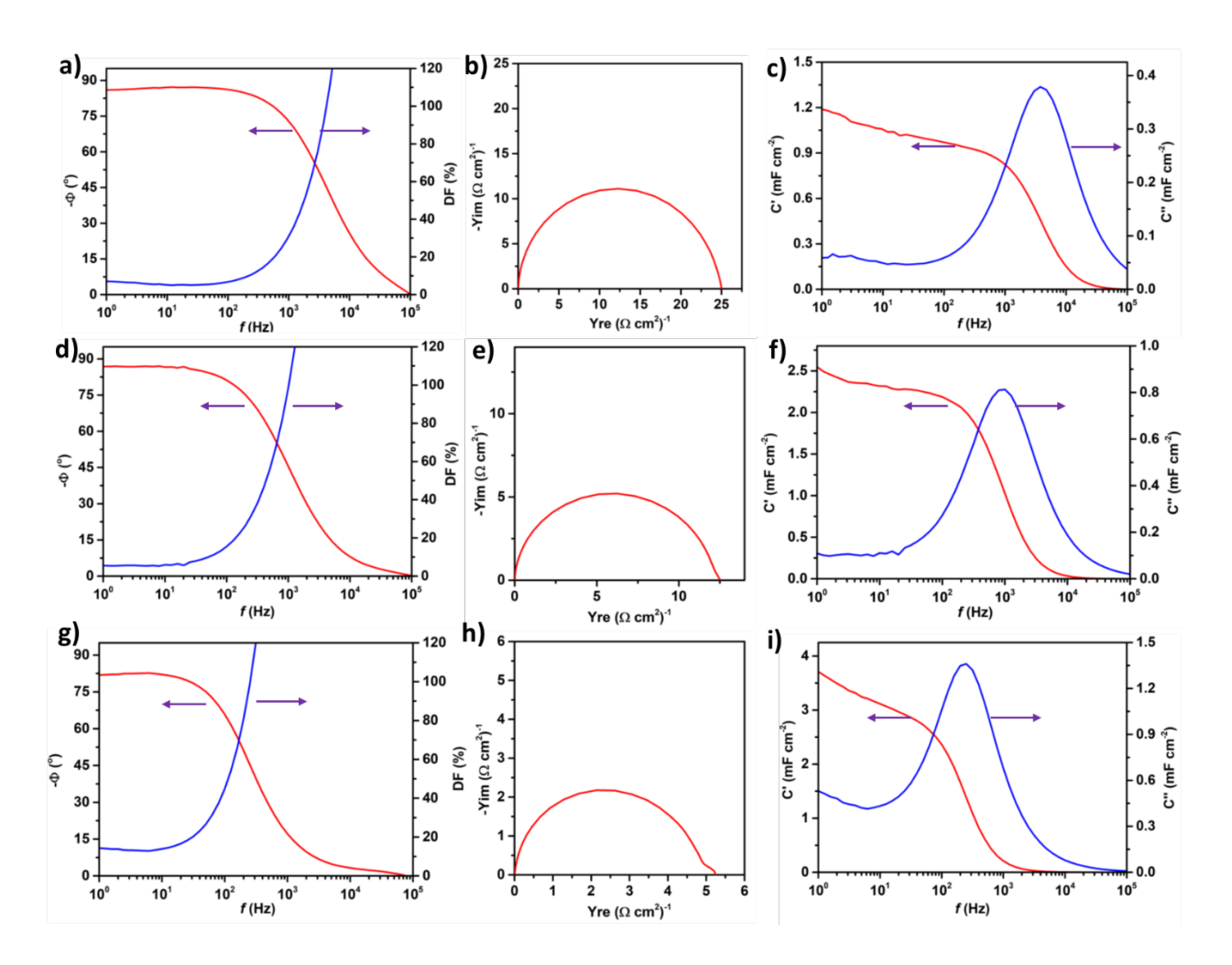


Figure S14. Phase angle and dissipation factor (DF) as functions of frequency (a, d, g), admittance-plane representation of EIS (b, e, h), and the real and imaginary parts of the complex capacitance as functions of frequency (c, f, i). (a-c) are for 3-GPB-5, (d-f) are for 4-GPB-5, and (g-i) are for 5-GPB-5 cell.

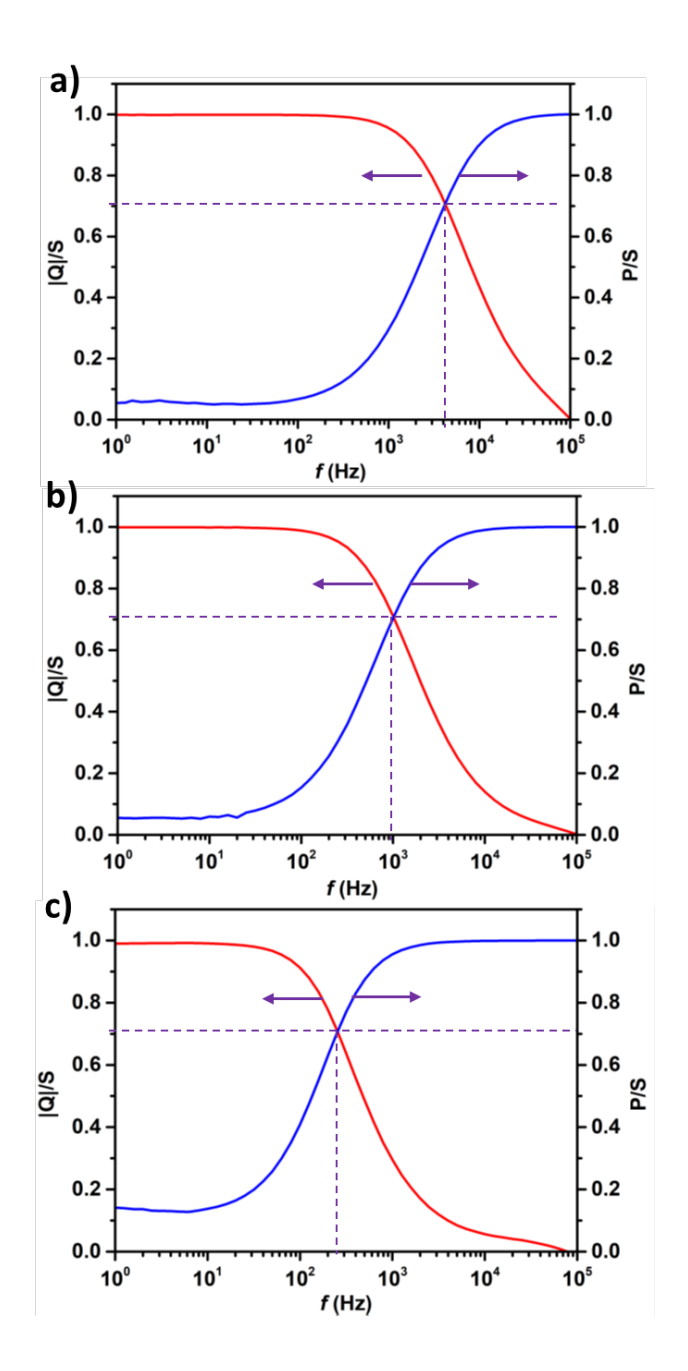


Figure S15. The normalized reactive power |Q|/S and the normalized power P/S as functions of frequency: (a) for 3-GPB-5, (b) for 4-GPB-5, and (c) for 5-GPB-5 cell.

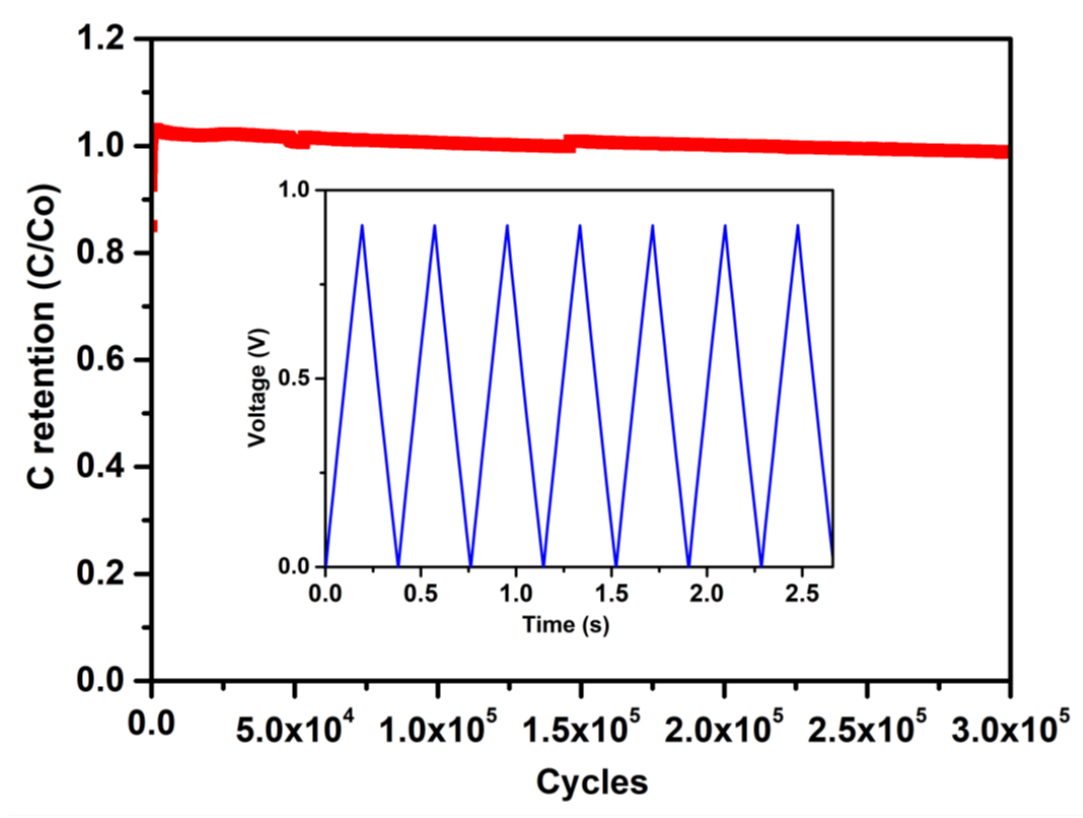


Figure S16. The long-term stability test was performed at 10 mA cm⁻². Its specific discharge capacitance only slightly decreased to ~95% after 300,000 cycles with the coulombic efficiency maintained at 100%, proving that this electrode material has great potential in long term stability. The slight capacitance degradation, in fact, most likely is related to the electrolyte decomposition at 0.9 V. Slightly lower voltage is necessary for much longer cycling lifetime. It is also noted that for ripple current filtering, ripple voltage is typically small, and charge-discharge only takes places at much less depth than the 100% depth tested here.

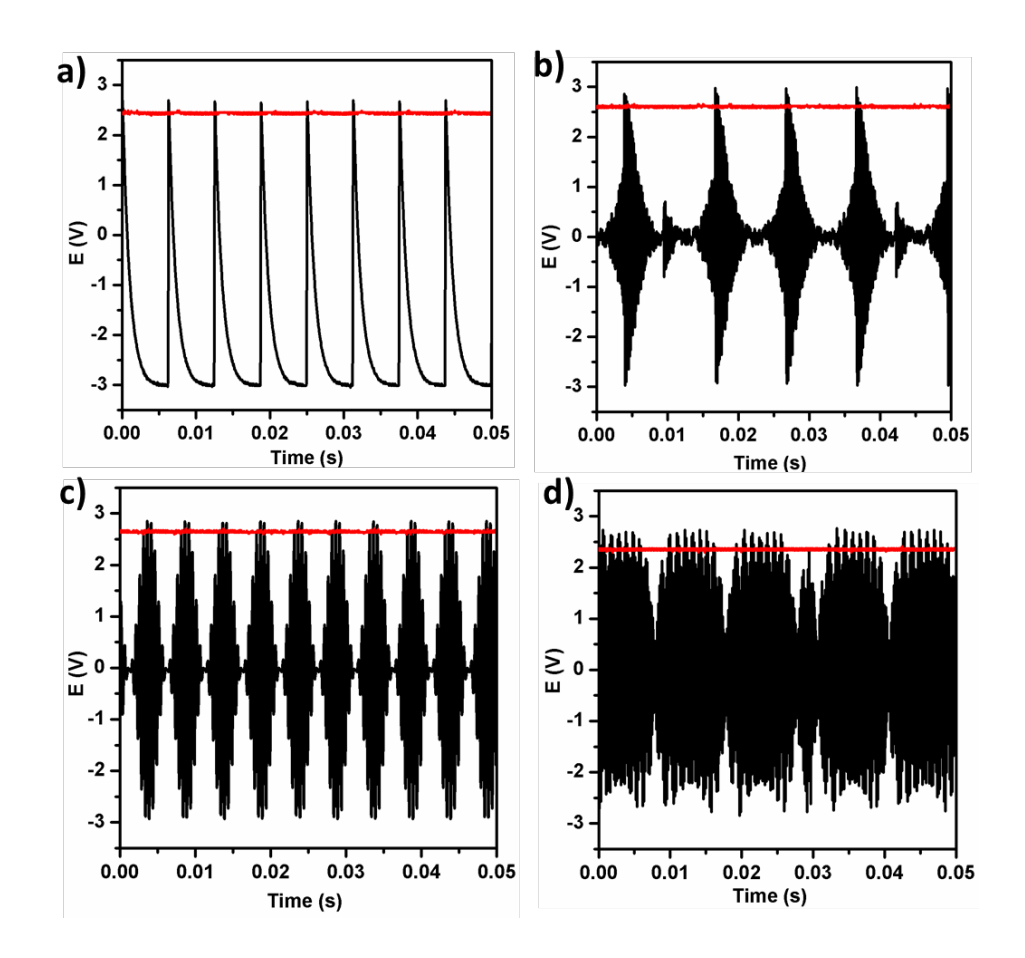


Figure S17. The experimentally measured output DC wave for the AC/DC converter at $1M\Omega$ load when the input is a different wave noise.

4. AC/DC Conversion and Ripple Voltage

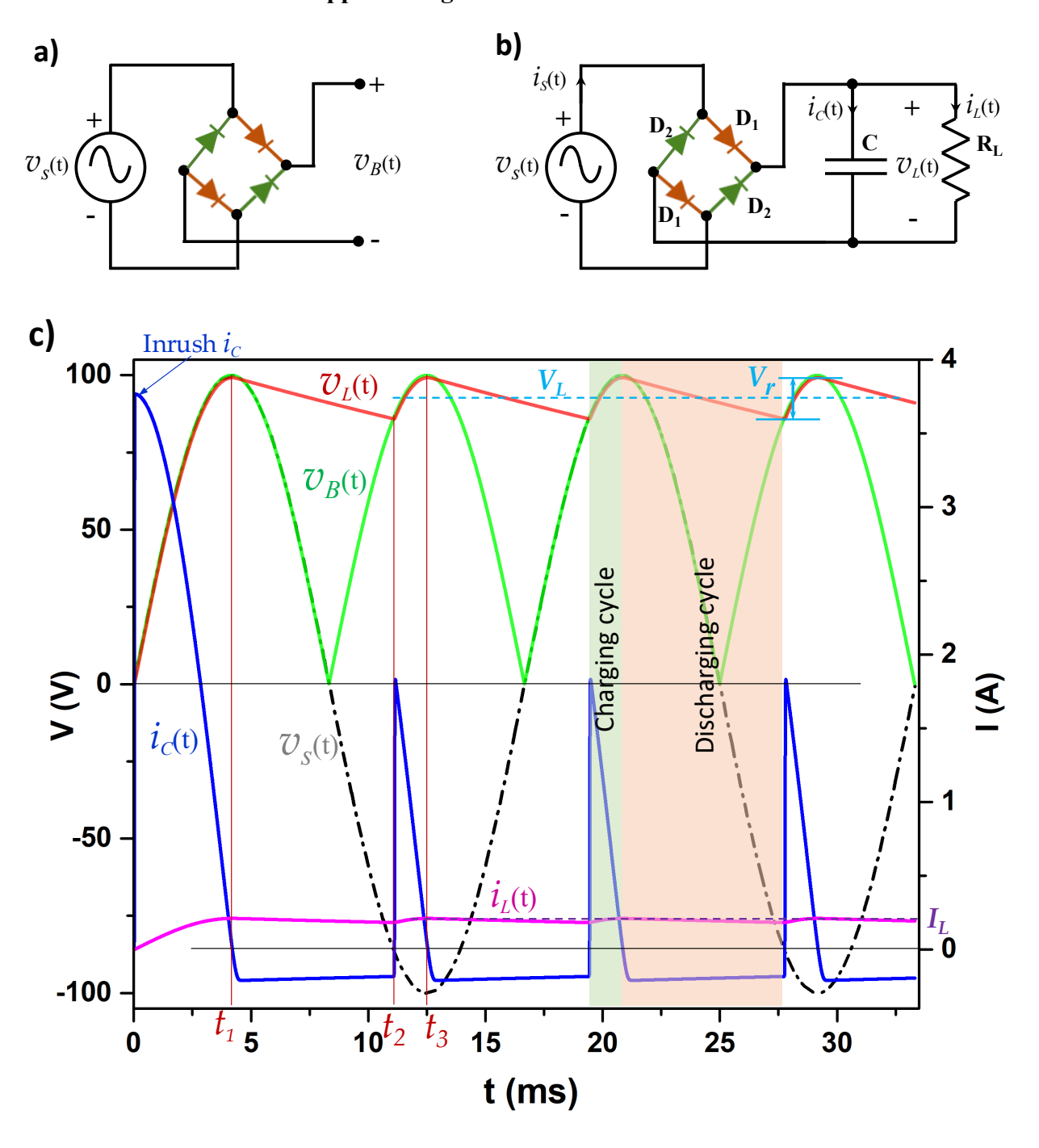


Figure S18. Schematics of AC/DC conversion for (a) full-bridge rectifier with an open circuit and (b) with the filtering capacitor and the load connected. (c) Simulated voltages and currents labeled in (a) and (b), for the case of $V_{\rm m} >> V_{\rm D}$.

In a conventional full-wave AC/DC converter (Figure S14a-b), the input sinusoidal AC source $v_s(t) = V_m \sin(\omega t)$ at 60 Hz line frequency is rectified by the diode bridge and then smoothed by the filtering capacitor C so that a steady DC voltage is delivered to the load R_L . Due to charge and discharge in the capacitor, the voltage across the capacitor, and hence the load voltage $v_L(t)$ always have variation, or the ripple component. The filtering capacitor should be properly selected, with a <u>practical</u> large capacitance, to reduce the ripple voltage or current to an allowable range for a given load.

4.1 General process in AC/DC conversion

As a generic example, we assume $V_{\rm m}=100~{\rm V},~C=0.1~{\rm mF},~R_L=0.47~{\rm k}\Omega$, and the voltage drop on one pair of diodes at on-state in the bridge rectifier $V_{\rm D}<\sim1{\rm V}$ so that $V_{\rm D}<< V_{\rm m}$. Figure S18c shows the simulated voltages and currents using PSpice tool. $v_B(t)$ is the rectified output from the diode bridge when no filtering capacitor and load is connected (Figure S18a). In the positive half cycle of $v_s(t)$, one pair of diodes D_1 - D_1 forms the current path and $v_B(t)$ traces $v_s(t)$; in the negative half cycle of $v_s(t)$, the other pair of diodes D_2 - D_2 forms the current path and $v_B(t)$ inverts the polarity of $v_s(t)$. Without any loads connected (no current), there is no voltage drop on the pair of diodes and hence $v_B(t) = |v_S(t)|$.

Now consider Figure S18b with the filtering capacitor and the load connected into the circuit: a) $0 \le t \le t_1$ (Initial charging)

In the first half cycle, D1-D1 is on, and a huge rush-in current $i_C(t)$ will charge the capacitor starting from 0 V, and $v_L(t)$ will trace the sinusoidal wave to $t_I \approx T/4$, where T is the period of the sinusoidal wave. Note that t_I could be slightly larger than T/4 if the initial R_LC discharge rate is too high. Meanwhile, the source $i_s(t)$ will also supply the load current $i_L(t) = v_L(t)/R_L$ and $i_s(t) = i_C(t) + i_L(t)$. Also note that with current flow in the diode pair and hence small voltage drop, the peak value of $V_L = v_L(t_1)$ is slightly less than $v_s(t_1)$.

b) $t_1 \le t \le t_2$ (Discharging)

Now all the diodes are off $(i_s(t) = 0)$ and the capacitor discharges to supply the load current with $i_c(t) = -i_L(t) < 0$ following

$$v_L(t) = V_L \exp(-t/\tau) \tag{31}$$

where $\tau = R_L C$, and $i_L(t) = v_L(t)/R_L$, with the load voltage and the current ramp down.

c) $t_2 \le t \le t_3$ (Charging)

In the 2nd half cycle at $t = t_2$, $v_s(t) > v_L(t)$, so the 2nd pair of diodes D₂-D₂are forwarded biased and turned on. The source current $i_s(t)$ starts to flow in to charge the capacitor and supply the load current: $i_C(t) > 0$ and $i_L(t)$ ramps up.

d) $t_3 \le t$ (Steady state charging and discharging cycles)

The system quickly enters a steady state for charging and discharging cycles. Because of the charge and discharge cycle, the load voltage contains a small AC component called ripple, and the amplitude of the ripple voltage V_r is the difference of the maximum and the minimum of $v_s(t)$, as shown in Figure S18c. The corresponding ripple current amplitude $I_r = V_r/R_L$.

It is desirable to minimize the ripple amplitude in the load, so a largest capacitance value that is <u>practical</u> is selected. In the extreme case $(C \to \infty)$, the duration of charging approaches to 0, and the duration of discharging approaches to the whole half cycle (T/2). The charge removed from the capacitor in one discharge cycle is

$$Q \approx \frac{I_L T}{2} \tag{32}$$

where I_L is the average load current. This amount of charge causes the capacitor voltage drop by V_r , and hence

$$Q = CV_r \tag{33}$$

Equating (32) and (33) allows us to solve for *C*:

$$C \cong \frac{I_L T}{2V_r} \tag{34}$$

It is emphasized that this equation (34) is approximate when the ripple is small.

The average voltage supplied to the load is approximately between the minimum and maximum of $v_s(t)$ in steady state:

$$V_L \cong V_{\rm m} - V_D - \frac{V_r}{2} \cong V_{\rm m} - \frac{V_r}{2} \tag{35a}$$

where V_D is the voltage on one pair of diodes in the on-state ($V_D \ll V_m$ in this example).

4.2 Low voltage AC/DC conversion

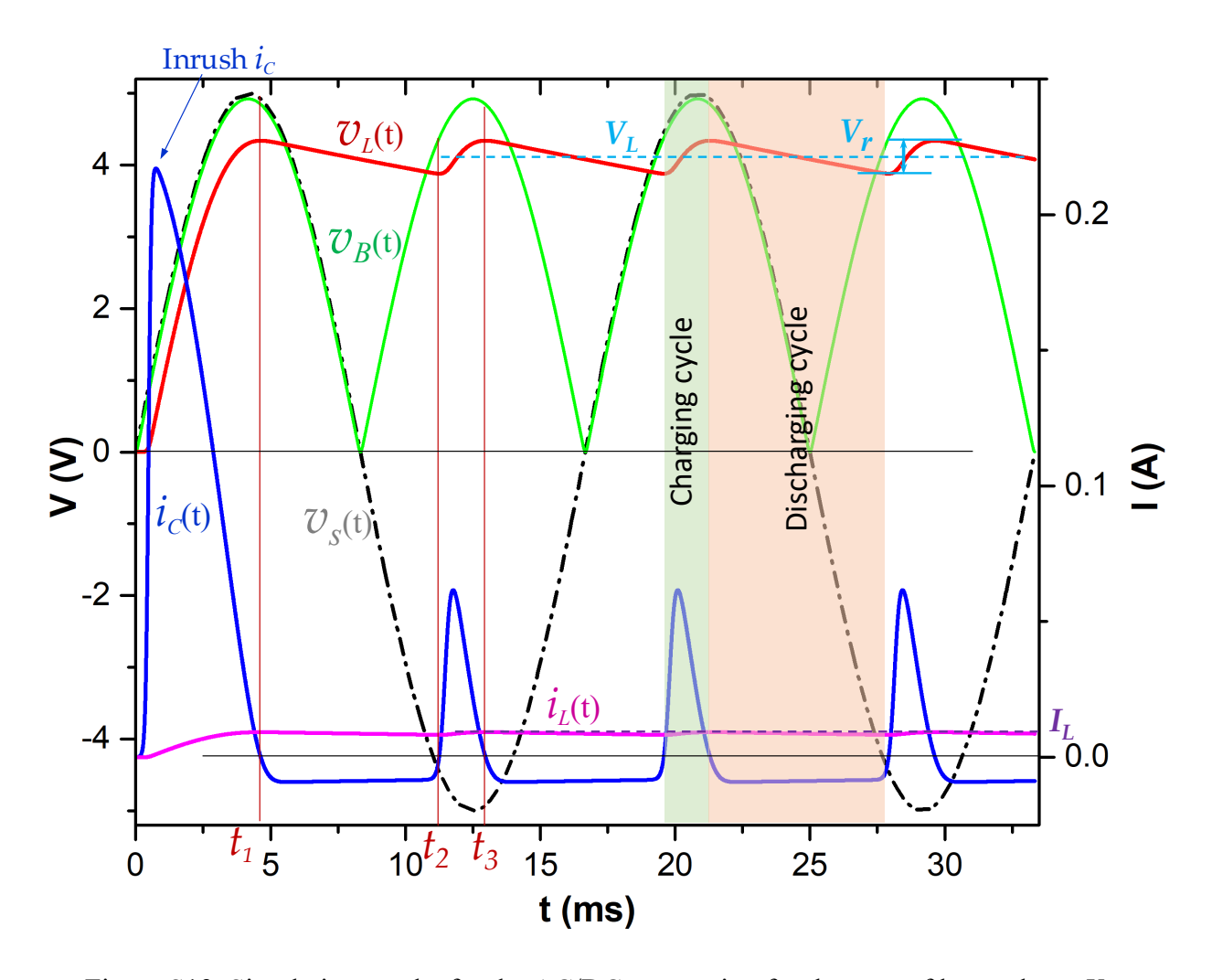


Figure S19. Simulation results for the AC/DC conversion for the case of low voltage $V_{\rm m}$.

In the above generic case (Figure S18c), it was assumed $V_{\rm m} >> V_{D} \sim 1$ V. However, for low voltage conversion, we cannot make this assumption. Figure S19 depicts such a case, where $V_{\rm m} = 5$ V, C = 0.1 mF, and $R_L = 0.47$ k Ω , and $V_{\rm D}$ is on the same order of magnitude as $V_{\rm m}$. Comparing to Figure S18c, it can be noticed that

- The inrush current reaches its peak value at a much-delayed time due to the delayed turn-on of the diode pair D1-D1.
- t_1 , t_2 and t_3 all are delayed, and particularly t_1 and t_3 occur at a moment after the source passes its peak V_m .
- The peak of $v_L(t)$ and hence its average V_L is less than V_m by $\sim 20\%$, corresponding to the value of $V_D \sim 1$ V.
- Equations (31-34) are still true, but (35a) should be modified as

$$V_L \cong V_{\rm m} - V_D - \frac{V_r}{2} \tag{35b}$$